

Deterministic and Probabilistic Tractography based on Complex Fibre Orientation Distributions

Maxime Descoteaux, Rachid Deriche, Thomas R. Knösche, and Alfred Anwander

Abstract—We propose an integral concept for tractography to describe crossing and splitting fibre bundles based on the fibre orientation distribution function (ODF) estimated from high angular resolution diffusion imaging (HARDI). We show that in order to perform accurate probabilistic tractography, one needs to use a fibre ODF estimation and not the diffusion ODF. We use a new fibre ODF estimation obtained from a sharpening deconvolution transform (SDT) of the diffusion ODF reconstructed from q-ball imaging (QBI). This SDT provides new insight into the relationship between the HARDI signal, the diffusion ODF, and the fibre ODF. We demonstrate that the SDT agrees with classical spherical deconvolution and improves the angular resolution of QBI. Another important contribution of this paper is the development of new deterministic and new probabilistic tractography algorithms using the full multidirectional information obtained through use of the fibre ODF. An extensive comparison study is performed on human brain datasets comparing our new deterministic and probabilistic tracking algorithms in complex fibre crossing regions. Finally, as an application of our new probabilistic tracking, we quantify the reconstruction of transcallosal fibres intersecting with the corona radiata and the superior longitudinal fasciculus in a group of 8 subjects. Most current DTI-based methods neglect these fibres, which might lead to incorrect interpretations of brain functions.

Keywords: fibre tractography, diffusion tensor imaging (DTI), anatomical connectivity, crossing fibres, high angular resolution diffusion imaging (HARDI), q-ball imaging (QBI), spherical deconvolution (SD), orientation distribution function (ODF).

I. INTRODUCTION

Diffusion-weighted (DW) magnetic resonance imaging (MRI) tractography is the only non-invasive tool available to obtain information about neural architecture of human brain white matter. This technique is

potentially very useful for the study of anatomical and functional brain relationships as well as for the discovery of functional distinctions between cortical regions of the brain. It is also important for the characterization of neuro-degenerative diseases, for surgical planning and for many other medical applications [1]. Currently, white matter fibre tractography is most commonly implemented using the principal diffusion direction of the diffusion tensor (DT). The (DT) model [2] characterizes the orientation dependence of the diffusion probability density function (PDF) of water molecules. An important limitation of the DT model arises from the Gaussian diffusion assumption which states that there can only be a single fibre population per voxel. At the resolution of DW-MRI acquisitions, this is quite a limiting assumption because many voxels have a low anisotropy index due to non-Gaussian diffusion arising from multiple fibre crossings, branching, fanning, and bottleneck formations. In fact, the resolution of DW-MRI acquisitions is usually between 3 mm^3 and 15 mm^3 , while the diameter of bundles of axons considered in fibre tractography are on the order of 1 mm (individual physical fibres are on the order of $1\text{--}30 \text{ }\mu\text{m}$ [1]). Furthermore, a recent study estimates that one-third of white matter voxels contain more than one fibre bundle orientation [3]. Thus, tractography algorithms based on the DT can follow false tracts due to diffusion profiles that are prolate or they can prematurely stop in regions with isotropic tensors.

To overcome these limitations of the DT, new High Angular Resolution Diffusion Imaging (HARDI) techniques have been developed. Good reviews can be found in [4], [5]. Most of these methods produce representations of water molecule diffusion as a function of direction such as in the cases of Diffusion Spectrum Imaging (DSI) [6], Q-Ball Imaging (QBI) [7], Composite Hindered and Restricted Model of Diffusion (CHARMED) [8], Persistent Angular Structure (PAS) [9] Diffusion Orientation Transform (DOT) [10] and multi-tensor distributions [11], [12]. Application of each of these methods results in various representations of the angular diffusion profile. For example, the principal

Copyright (c) 2008 IEEE. Personal use of this material is permitted. However, permission to use this material for any other purposes must be obtained from the IEEE by sending a request to pubs-permissions@ieee.org.

M. Descoteaux is with the NMR Lab, NeuroSpin, CEA / Saclay, France, R. Deriche is with the Odyssée Project Team, INRIA Sophia Antipolis - Méditerranée, France and T. Knösche and A. Anwander are with the Max Planck Institute for Human Cognitive and Brain Science, Leipzig, Germany.

directions extracted from the Orientation Distribution Function (ODF) [7] can be interpreted as principal directions of the underlying fibre architecture. Alternatively, there have been a number of attempts to directly estimate the distribution of the fibre directions within a voxel (fibre ODFs) using spherical deconvolution (SD) or mixture models. These methods need explicit assumptions about the contribution of a single fibre or fibre bundle to the measured signal and are extensively reviewed in [4].

We present a methodological framework that explicitly links the diffusion ODF with the fibre ODF by subjecting the former to a sharpening deconvolution transform (SDT). The results obtained using this new fibre ODF derived from the Q-Ball diffusion ODF largely agree with the outcome of classical approaches to fibre ODF computation [13]. This allows for a direct comparison between the diffusion ODF that is used by many researchers (e.g. [11], [14], [15], [16], [17]) and the fibre ODF corresponding to it. Furthermore, this new fibre ODF can be seen as a way to improve the angular resolution of QBI and thus improve accuracy of probabilistic tractography. By partitioning the process of estimating the fibre ODF into its two natural sub-processes, computation of the diffusion profile from measured DW signals and model-based reconstruction of the fibre ODF from the diffusion ODF, we gain a deeper understanding of the modeling procedure. Influences on and sensitivities of the two processing steps can be studied separately. We may evaluate intermediate results and therefore assess how improvements/alterations in the data and procedure (such as better signal to noise ratios, alterations of b-values, improvements in regularization, more gradient directions, etc.) are received.

In order to better deal with fibre crossings in tractography, HARDI-based techniques are needed. Two families of tractography algorithms exist: those that are deterministic and those that are probabilistic. Research groups have recently started to generalize both deterministic and probabilistic DT-based tracking algorithms in order to use some of the HARDI reconstruction methods mentioned above. Popular high order functions used in the literature are estimates of the diffusion ODF, the PAS function [18], variants of multi-tensor fitting models [19], [20], [3], [21], and parametric Spherical Deconvolution (SD) [22]. These techniques improve tracking results when the DT model fits the data poorly. They have been shown to reconstruct some crossing and branching fibre bundles. In this paper, we introduce new deterministic and probabilistic tractography algorithms that use the diffusion ODF obtained by QBI and the fibre ODF estimated by SDT. We show that one need to use a fibre ODF rather than the diffusion ODF in order to

perform accurate probabilistic tractography estimation. In particular, we illustrate the relationship between the DW signal, diffusion ODF and fibre ODF.

To our knowledge, no explicit comparison between the two families of HARDI-based tracking methods (deterministic and probabilistic) has been performed. Another contribution of this paper is therefore to experimentally examine differences between our new deterministic and probabilistic tracking algorithms.

In order to illustrate the contributions of our new tracking algorithms, we focus on brain regions with complex fibre architecture such as projections of callosal fibres to the cortex. These bundles have been studied extensively in the neuroanatomical and DTI literature (e.g. [32]). The corpus callosum (CC) is involved in the interhemispheric interaction between cortical regions and the reconstruction of fibres connecting the cerebral hemispheres is of major interest for cognitive research and clinical practice. While DT-based tractography finds fibres passing through the CC connected with the medial/dorsal cortex, lateral and ventral fibres are not found because they cross the corona radiata and the superior longitudinal fasciculus (SLF). Only a recently has a study [33] proposed to use a HARDI-based method to reconstruct fibres of the genu and splenium of the CC. Hence, a further contribution of this paper is the reconstruction of the transcallosal fibres of multiple subjects.

The paper is outlined as follows. In Section II, we review relevant tractography background literature to illustrate and motivate our new deterministic and probabilistic algorithms. We then review our fast, regularized and analytical ODF estimation [23] in Section III-A and develop the SDT that produces sharp fibre ODFs in Section III-B. The deterministic and probabilistic tractography algorithms are developed in Sections III-C and III-D, respectively. Then, we present qualitative and quantitative evaluations of the SDT and compare performance of the algorithms on several white matter regions with complex fibre architecture in Section IV. Finally, we conclude with a discussion of the results and directions for future work in Section V.

II. TRACTOGRAPHY OVERVIEW

The most intuitive tracking algorithms are the classical deterministic Streamline (STR) tracking algorithms [24], [25], [26] and the slightly more complex Tensor Deflection (TEND) algorithms [27], [28] used in many applications. Other DT-based streamlines and flow-based approaches are reviewed in [1]. Here, we focus on HARDI-based tractography algorithms.

Recently, in [11], [17] a generalized streamline tracking algorithm was proposed based on the principal direction of the diffusion ODF computed from DSI. In [19]

and in [29], a multi-tensor local model of the data is used to extend the fibre assignment by the continuous tracking (FACT) [24] algorithm, and in [30], multiple maxima of the q-ball ODF are used to also extend FACT into a multiple ODF maxima FACT (M-FACT). To deal with more complex fibre configurations, [31] extended streamline tracking by using a mixture of Gaussian densities. Similarly, [20] recently extended the TEND model with a bi-Gaussian model. Finally, based on the classical diffusion ODF reconstructed from QBI [7] and a regularized version of the diffusion ODF [16], [32], proposed an extension of the streamline to deal with fibre crossings. In this chapter, we propose another extension to streamline tractography based on the multiple maxima information of the fibre ODF. From this fibre ODF, we extract all available maxima and allow for splitting in multiple directions at each step. Not only can the tracking propagate through crossing fibres, but it can also deal with fanning and branching fibre bundles.

Existing deterministic HARDI-based techniques mostly show that tracking is improved compared to tensor based tracking, when the DT model fits the data poorly. However, these deterministic tractography algorithms inherit the classical limitations of deterministic algorithms such as choice of initialization [33], sensitivity to the estimated principal direction, lack of a straightforward way to compute statistics on tracts, and lack of connectivity information between regions of the brain [11]. To overcome limitations of deterministic tractography, DT-based probabilistic [34], [31], [35], [36], [37], [21] and geodesic [38], [39] algorithms have been used. This also motivates the development of new HARDI-based probabilistic algorithms. Probabilistic algorithms are computationally more expensive than deterministic ones, but can better deal with partial volume averaging effects and noise in the estimated fibre directions. Most importantly, the outputs of probabilistic algorithms are usually designed to give a connectivity index measuring how probable it is that two voxels are connected to one another.

HARDI-based probabilistic tractography methods have recently been generalized to several existing DT-based methods [15], [18], [3], [40], [30], [41], [42], [22], [43]. First, in [22] parametric spherical deconvolution is used and in [3], a mixture of Gaussian models is used to extend the probabilistic Bayesian DT-based tracking [35]. Related to these techniques, [40] uses a Bayesian framework to do global tractography instead of tracking through local orientations. In [15], Monte Carlo particles move inside the continuous field of q-ball diffusion ODF and are subject to a trajectory regularization

scheme. In [18], [42], an extension to a DT-based approach [31] is proposed using a Monte Carlo estimation of the white matter geometry. Their implementation is based on PAS-MRI with a noise modeling component and more recently they use a Bingham distribution to model peak anisotropy in the fibre distributions [41]. In [30], large numbers of M-FACT QBI streamlines are reconstructed and then all pathways are reverse-traced from their end points to generate a map of connection probabilities. Overall, these methods show successful tracking of several fibre bundles that are difficult to recover when using DT-based techniques. Although [41] does take fanning configurations into consideration, most of these methods mainly focus on fibre bundles with crossing configurations and do not attempt to account for bundles demonstrating high curvature or points where fibre populations branch or fan. In this paper, our probabilistic algorithm attempts to account for branching and fanning fibre populations as well as fibre crossings. The novelty is to use the fibre ODF.

Normally, an advantage of the probabilistic tractography techniques is that they are based on full spherical functions (such as DT, ODF, PAS, etc.) and not on the principal direction or extracted maxima alone. However, this creates problems when the spherical function profiles represent diffusion rather than fibre directions. These profiles are often overly smooth and have significant isotropic components due to the fact that not all water diffusion takes place along the directions of the nerve fibres. In this case, tractography may produce diffuse results that suggest connections in unexpected regions of the white matter. This is a well-known problem in probabilistic DT tractography and has not been thoroughly studied in the literature. Typically, it is tackled somewhat heuristically, e.g. by simply taking a power of the diffusion tensor [27], [34], [44], [45] to increase the ratio of largest to smallest eigenvalue and thus obtain more elongated tensors. However, a much better way to avoid diffusive tracking and leaking in probabilistic tractography is to use the fibre ODF. The exact relationship between diffusion ODF and fibre ODF is complicated and depends upon the diffusion properties of the single fibres. It is currently an open area of study in the field [11], [15]. However, there are techniques based upon the use of spherical deconvolution (SD) [13], [46], [47], [48], [49], [50], [22], [4] that attempt to reconstruct the fibre ODF (also called the Fibre Orientation Density FOD) using the assumption that the DW signal profile measured for a single fibre population does not vary between different fibre bundles.

From the above, it follows that study of the relationship between the orientation density function of water

diffusion and the orientation density function of nerve fibres within a DW-MRI voxel is interesting. This is why we propose a new ODF deconvolution operation that has the effect of transforming the diffusion ODF into a sharper fibre ODF. To validate this approach, we extensively compare our new fibre ODF with the classical FOD estimated from SD [13].

III. METHODS

In this section, we introduce our analytical solution to QBI developed in [23], our sharpening deconvolution transform (SDT), and our new deterministic and probabilistic tracking algorithms.

A. Analytical Regularized ODF from QBI

Tuch [7] demonstrated that the ODF could be estimated directly from raw HARDI measurements on a single sphere by a numerical implementation of the Funk-Radon transform (FRT). We have showed in [23] that this FRT can be solved analytically, robustly, and more quickly. The key is to express the HARDI signal as a spherical harmonic (SH) series of order ℓ and then solve the FRT using the Funk-Hecke theorem. Note that Anderson [47] and Hess et al. [51] have recently developed a similar analytical solution for the ODF reconstruction in QBI. Despite the fact that our analytical solution is similar to theirs, our regularized estimation part, our derivation, our experimental results, and our validations of the solution are quite different as is clearly demonstrated in [23].

In our analytical QBI solution, the signal at position p is first estimated as

$$S(\mathbf{u})_p = \sum_{j=1}^R c_j Y_j(\mathbf{u}), \quad (1)$$

where $S(\mathbf{u})$ is the measured diffusion weighted signal in each of the N gradient directions $\mathbf{u} := (\theta, \phi)$ on the sphere (θ, ϕ obey physics convention, $\theta \in [0, \pi], \phi \in [0, 2\pi]$), c_j are the SH coefficients describing the signal, Y_j is the j^{th} element of the SH basis and $R = (1/2)(\ell + 1)(\ell + 2)$ is the number of terms in the basis of order ℓ when choosing only even orders. Our implementation is based on a modified symmetric, real, orthonormal basis and the coefficients c_j are obtained with a Laplace-Beltrami regularization least-square approach in order to eliminate unnecessary high order terms in the SH approximation [52]. Note that this kind of regularization was also applied with success to the FOD estimated with spherical deconvolution in [49] using a gradient constraint instead of a Laplace-Beltrami

constraint. The exact Laplace-Beltrami regularized expression for the coefficients c_j is given in [52, Eq.15]. Our Laplace-Beltrami regularization involves using the right operator for the space of functions of the unit sphere and yields better estimations and more robust fibre detections [23] than without regularization [47] or with classical Tikhonov regularization [51].

Spherical harmonics allow the simplification of the Funk-Radon Transform (FRT) by the Funk-Hecke theorem. The final ODF reconstruction, Ψ , at position p , is simply a diagonal linear transformation of the signal SH coefficients c_j ,

$$\Psi(\mathbf{u})_p = \sum_{j=1}^R 2\pi P_{\ell_j}(0) c_j Y_j(\mathbf{u}), \quad (2)$$

where ℓ_j is the order associated with j^{th} SH basis element (for $j = \{1, 2, 3, 4, 5, 6, 7, \dots\}$, $\ell_j = \{0, 2, 2, 2, 2, 2, 4, \dots\}$) and $P_{\ell_j}(0)$ a Legendre polynomial with simple expression since we use only even orders in the SH basis,

$$P_{\ell_j}(0) = (-1)^{\ell_j/2} \left(\frac{3 \cdot 5 \cdots (\ell_j - 1)}{2 \cdot 4 \cdots \ell_j} \right). \quad (3)$$

B. The Sharpening Deconvolution Transform (SDT) and the Fibre ODF

The diffusion ODF as produced by QBI has the disadvantage that it represents the motion of water molecules which often but not exclusively diffuse parallel to the fibre. This renders the resulting profiles overly smooth. The relationship between the diffusion ODF and the fibre ODF can depend on the physics of diffusion, the cell membrane permeability, the free diffusion coefficients, the axonal packing, the distribution of axonal diameters and the degree of myelination in the underlying fibre bundles. It is therefore very difficult to be absolutely sure about its form. However, it can be assumed that (1) the fibre ODF is sparse in the sense that the fibres are organized in bundles, and (2) some of the diffusion represented by a Q-ball is not in the direction of the underlying nerve fibres. This implies that the underlying fibre ODF ought to be sharper than the observed diffusion ODF. Here, we describe the sharpening operation called spherical deconvolution transform (SDT) that transforms the smooth diffusion ODF into a sharper fibre ODF. This transform makes explicit the relationship between the directions of the nerve fibres (fibre ODF), the diffusion of the water molecules influenced by those fibres (diffusion ODF), and the MR signal attenuation caused by the diffusion.

The SDT is a simple linear transformation of the spherical harmonic (SH) coefficients describing the diffusion ODF. We use spherical deconvolution (SD). Our

approach is inspired by the original SD approach proposed by Tournier et al. [13] in which the measured signal is expressed as the convolution on the unit sphere of the fibre response function with the FOD [13, Fig.1]. Assuming a particular fibre response function representing the diffusion signal attenuation that would be measured for a single fibre, [13] demonstrates that the deconvolution of the signal with the response function gives the FOD. This was also recently employed by others in [47], [49], [50], [48]. Here, the starting point is not the measured signal, but is rather our estimated diffusion ODF described in Section III-A. The diffusion ODF contains information about the fibre ODF, but this information is “*blurred out*” by the diffusion process. To extract this fibre information, it is therefore necessary to deconvolve the estimated smooth diffusion ODF Ψ , by a certain diffusion ODF kernel for a single fibre in order to obtain a sharper ODF that we will call Ψ_{sharp} . The procedure is sketched in Fig. 1.

[Fig. 1 about here.]

We assume that the estimated diffusion ODF Ψ is formed by convolution between the single fibre diffusion ODF kernel, R , and the true fibre FOD. Hence, the deconvolution of the diffusion ODF by the diffusion ODF kernel can recover a sharper fibre ODF.

The convolution on the sphere between R and Ψ_{sharp} (Fig. 1a) can be written as

$$\Psi(\mathbf{u}) = \int_{|\mathbf{w}|=1} R(\mathbf{u} \cdot \mathbf{w}) \Psi_{\text{sharp}}(\mathbf{w}) d\mathbf{w}. \quad (4)$$

In order to solve this integral, we first replace Ψ and Ψ_{sharp} with their respective SH estimations of order ℓ , $\sum_j c_j Y_j(\mathbf{u})$ and $\sum_j c_{j\text{sharp}} Y_j(\mathbf{u})$ and obtain

$$\sum_{j=1}^R c_j Y_j(\mathbf{u}) = \sum_{j=1}^R c_{j\text{sharp}} \int_{|\mathbf{w}|=1} R(\mathbf{u} \cdot \mathbf{w}) Y_j(\mathbf{w}) d\mathbf{w}.$$

At this point, we use the Funk-Hecke theorem described in Appendix A to solve the integral over the sphere between R and the spherical harmonic Y_j . The Funk-Hecke formula is a theorem that relates the inner product of any spherical harmonic with any continuous function defined on the interval $[-1, 1]$. Use of the Funk-Hecke formula is also at the core of our analytical ODF estimation presented in Section III-A [23]. Hence, we obtain

$$c_{j\text{sharp}} = \frac{c_j}{f_j}, \quad \text{where} \quad f_j = 2\pi \int_{-1}^1 P_{\ell_j}(t) R(t) dt, \quad (5)$$

P_{ℓ_j} is a Legendre polynomial of order ℓ_j and coefficients f_j come from the Funk-Hecke formula, which is

expanded in Eq. 13 of Appendix A. Therefore, the final sharp fibre ODF expression at position p is given by

$$\Psi_{\text{sharp}}(\mathbf{u})_p = \sum_{j=1}^R 2\pi P_{\ell_j}(0) \frac{c_j}{f_j} Y_j(\mathbf{u}). \quad (6)$$

For the rest of the paper, we refer to this ODF as the fibre ODF (fODF).

From Eq. 6, note that the fibre ODF estimate is obtained from a concatenation of two operators. First, the HARDI signal c_j is transformed by $2\pi P_{\ell_j}(0)$ into the diffusion ODF and then, transformed by $1/f_j$ into the fibre ODF. It is important to point out that in classical HARDI SD [13], the fibre ODF or FOD is obtained in a single step that transforms the HARDI signal coefficients directly. Hence, classical SD is more direct, but our method provides a new way to think about spherical deconvolution and will be appealing to many researchers who are used to thinking in terms of the diffusion ODF.

The main choice to be considered in this analysis is in the creation of a viable diffusion ODF kernel R . Assuming that a Gaussian can describe the diffusion of water molecules for a single fibre, we choose a prolate tensor profile with eigenvalues $e_1 \geq e_2 = e_3$ to represent this Gaussian. This is the same symmetric prolate tensor assumption that is used in [47]. It has the advantage of having an analytical diffusion ODF [7], [23] expression which can be used to obtain our diffusion ODF kernel R . In the synthetic simulations of [13], [23] and in the model-based approach of [48], values for the diffusion profile are set according to physiologically-inspired measurements. Here, we prefer to estimate the diffusion ODF kernel directly from our real dataset (Tournier et al [13], [50] and Anderson [47] also estimate their single fibre response function from real data). All details are given in Appendix A where the analytical diffusion ODF kernel R is derived. In practice, the average prolate tensor profile is estimated from the 300 voxels with the highest FA values, as these tensors can each be assumed to contain a single fibre population.

C. Deterministic Multidirectional ODF Tracking

We extend classical streamline techniques [1], [25], [26] based on diffusion tensor principal directions to take into account multiple ODF maxima at each step. We denote $p(s)$ as the curve parametrized by its arc-length. This curve can be computed as a 3D path adapting its tangent orientation locally according to a vector field \mathbf{v} . Hence, for a given starting point p_0 , we solve $p(t) = p_0 + \int_0^t \mathbf{v}(p(s)) ds$. The integration is typically performed numerically with Euler or Runge-Kutta schemes of order 2 or 4. In the case of using Euler methods, we have the

discrete evolution equation

$$p_{n+1} = p_n + \mathbf{v}(p_n)\Delta s, \quad (7)$$

where Δs is a small enough step size to obtain subvoxel precision. A continuous linear, cubic, spline or geodesic [38] interpolation of the vector field can be performed at each step for the subvoxel points. A good review of deterministic tracking methods can be found in [1] and more recently in [5].

For our deterministic algorithm, we need one or more seed points, p_0 ; we need an anisotropy measure map A (FA, generalized FA GFA [7] or any other anisotropy measure); we need an anisotropy measure threshold t_{aniso} to make sure we stay within the white matter; we need a curvature threshold t_θ to make sure curves do not come back on themselves; we need a function $\text{ExtractMax}(\Psi, p)$ that returns the list l of directions l_j along each fibre ODF maxima Ψ' at point p ; and finally we need a function $\text{size}(l)$ that returns the size of list l . The deterministic fibre ODF tracking algorithm can be described as follows:

- (0) Estimate field of fODF, Ψ_{sharp} , with Eq. 6
- (1) **Set** seed p_0 and **set** $\mathbf{v}(p_0) = \text{argmax}_{\mathbf{u}} \Psi_{\text{sharp}}(\mathbf{u})_{p_0}$
- (2) Update curve according to Eq. 7.
 - If** $A(p_n) < t_{aniso}$ **then STOP**;
 - If** $\frac{\mathbf{v}(p_n) \cdot \mathbf{v}(p_{n-1})}{\|\mathbf{v}(p_n)\| \|\mathbf{v}(p_{n-1})\|} > t_\theta$ **then STOP**;
 - Let** $l = \text{ExtractMax}(\Psi_{\text{sharp}}, p_n)$. **If** $\text{size}(l) > 1$ **then SPLIT** curve; **for** $i = 1$ to $|l|$ **do** (1) with $p_0 = p_n$ and $\mathbf{v}(p_0) = l_i$;

ODF estimation is done using order $\ell = 4, 6$ or 8 as in [23] and the ODF kernel is estimated from our real dataset. It is generally assumed that ODF maxima are given by the local maxima of the normalized ODF ($[0,1]$), where the function surpasses a certain threshold (here, we use 0.5). In practice, we project the ODF onto the sphere tessellated with a fine mesh. We use a 16th order tessellation of the icosahedron that gives 1281 sample directions on the sphere. Then we implement a finite difference method on the mesh. If a mesh point is above all its neighbours and if that point has an ODF value above 0.5, we assign the mesh point direction to be a maximum. This thresholding avoids selecting small peaks that may appear due to noise. Other more complex methods exist to extract maxima such the method presented in [53] or spherical Newton's method [9].

In our implementation, we use FA and $t_{aniso} = 0.1$ as a mask to prevent tracks that leak outside white matter, we set curving angle threshold $t_\theta = 75^\circ$ and $\Delta s = 0.1$, and we use Euler integration with classical trilinear

interpolation to obtain dODF, fODF and DT at subvoxel precision. For the rest of the paper, DT-STR refers to the algorithm using the DT principal eigenvector, whereas dODF-STR and fODF-STR refer to the algorithm using a single dODF/fODF maximum that is the closest to the incoming tangent direction of the curve, and SPLIT-STR refers to the algorithm using all available fODF maxima with splitting at each step.

D. Probabilistic fibre ODF Tracking

In this section, we propose an extension of the random walk method proposed by Anwender et al. [45] and Koch et al. [34] in which we use the multidirectional fibre ODF. Imagine a particle in a seed voxel moving in a random manner with a constant speed within the brain white matter. The transition probability to a neighbouring point depends on the local fODF Ψ_{sharp} . This yields high transitional probabilities along the main fibre directions. Hence, the particle will move in parallel to the fibre direction with a higher probability than in a perpendicular direction. In this probabilistic method, we start a large number of particles from the same seed point, let the particles move randomly according to the local fODF and count the number of times a voxel is reached by the path of a particle. The random walk is stopped when the particle leaves the white matter volume.

For each elementary transition of the particle, the probability for a movement from the seed point x to the target point y in one of N directions, \mathbf{u}_{xy} , is computed as the product of the local fODFs in direction \mathbf{u}_{xy} , i.e. $P(x \rightarrow y) = \Psi_{\text{sharp}}(\mathbf{u}_{xy})_x \cdot \Psi_{\text{sharp}}(\mathbf{u}_{xy})_y$ where $P(x \rightarrow y)$ is the probability for a transition from point x to point y , $\Psi_{\text{sharp}}(\mathbf{u}_{xy})_x$ is the fibre ODF at point x in direction xy and $\Psi_{\text{sharp}}(\mathbf{u}_{xy})_y$ is the fibre ODF at point y in direction yx (by symmetry, directions xy and yx are the same).

The transition directions in the local model are limited to $N = 120$ discrete directions corresponding to the angular sampling resolution of the acquired data. The step size of the particle step was fixed at 0.5 times the voxel size. We used trilinear interpolation of the fODF for the subvoxel position. Voxels within the CSF and voxels containing mainly gray matter were excluded from the tracking using a mask computed from a minimum FA value of 0.1 and a maximum ADC value of 0.0015. These values were optimized to produce agreement with the white matter mask from the T1 anatomy. The mask was morphologically checked for holes in regions of low anisotropy due to crossing fibres. Finally, a total of 100,000 particles were tested for each seed voxel. The connectivity of any given voxel to the seed voxel was estimated by the number of particles that reached

the voxel. For the rest of this paper, the 3-dimensional image of the connectivity values is called a *tractogram*. To remove artifacts of the random walk, only voxels that were reached by at least 100 particles were used for further processing (thresholding). For visualization purposes, the dynamic range of the connectivity values were logarithmically transformed and the entire tractogram was normalized.

The main additions to the probabilistic algorithm compared to previously published versions [34], [45] are the use of the fODF after deconvolution of the diffusion data, the use of higher angular sampling combined with a continuous interpolation of the data, and the use of subvoxel streamline tracking. The deconvolution sharpening pre-processing step is shown to have a dramatic impact on the quality of the tractogram. For the rest of the paper, the method just described is referred to as fODF-PROBA.

E. Data Acquisition

1) *Synthetic Data Generation*: We generate synthetic ODF data using the simple multi-tensor model that leads to an analytical expression of the ODF [23]. For a given b -factor and noise level, we generate the diffusion-weighted signal $S(\mathbf{u}_i) = \sum_{k=1}^n p_k e^{-b\mathbf{u}_i^T \mathbf{D}_k \mathbf{u}_i} + \text{noise}$, where \mathbf{u}_i is the i^{th} gradient direction on the sphere, n is the number of fibres, p_k is the volume fraction of the k^{th} fibre and \mathbf{D}_k the k^{th} diffusion tensor profile oriented randomly. We use the tensor profile \mathbf{D}_k estimated directly on our real dataset using the 300 voxels with the highest FA. Finally, we add complex Gaussian noise with standard deviation of σ , producing a signal with a signal to noise ratio (SNR) of $1/\sigma$.

2) *Human Brain Data*: Diffusion weighted data and high-resolution T_1 -weighted images were acquired from eight healthy right-handed volunteers (25 ± 4 years old, four females) on a whole-body 3 Tesla Magnetom Trio scanner (Siemens, Erlangen) equipped with an 8-channel head array coil [45]. Written informed consent was obtained from all subjects in accordance with the ethical approval from the University of Leipzig. The spin-echo echo-planar-imaging sequence (TE = 100 ms, TR = 12 s, 128 x 128 image matrix, FOV = 220 x 220 mm²) consists of 60 diffusion encoding gradients [54] with a b -value of 1000 s/mm². Seven images without any diffusion weightings were placed at the beginning of the sequence and after each block of 10 diffusion weighted images to provide anatomical reference for offline motion correction. The measurement of 72 slices with 1.7 mm thickness (no gaps) covered the whole brain. Random variations in the data were reduced by averaging the data from three acquisitions, resulting in

an acquisition time of about 45 minutes. The SNR in the white matter of the S_0 images averaged from three acquisitions was estimated to be approximately 24. No cardiac gating was employed in order to limit the acquisition time. The issue of cardiac gating is discussed in [55]. Additionally, fat saturation was employed, a 6/8 partial Fourier imaging was used, a Hanning window filter was applied, and parallel acquisition (generalized auto-calibrating partially parallel acquisitions, reduction factor = 2) in the axial plane was used.

The brain is skull stripped from the T_1 -anatomy, which was aligned with the Talairach stereotactical coordinate system [56]. The 21 images without diffusion weighting distributed within the whole sequence were used to estimate motion correction parameters using rigid-body transformations [57] as implemented in [58]. The motion correction for the 180 diffusion-weighted images was combined with a global registration to the T_1 anatomy computed with the same method. The gradient direction for each volume was corrected using the rotation parameters. The registered images were interpolated to the new reference frame with an isotropic voxel resolution of 1.72 mm and the three corresponding acquisitions and corresponding gradient directions were averaged.

F. Evaluation of the SDT

1) *Spherical Deconvolution*: To justify the choice of our fODF, we also reconstructed the FOD using spherical deconvolution [13]. We implemented the filtered SD (fSD) [13] using spherical harmonics and a low-pass filter [1,1,1,0.8,0.1] multiplying each coefficient of order $\ell \in \{0, 2, 4, 6, 8\}$ respectively, as detailed in [13]. This filtering is introduced to reduce the effect of noise and spurious peaks produced by high order spherical harmonic coefficients of the FOD estimation. There are more recent versions of spherical deconvolution with regularization [49] and positivity constraints with super-resolution [50] that have just appeared in the literature. Here, we choose to compare our methods against the classical fSD [13] because it has been extensively studied in the literature and because the method is linear just like our proposed approach.

2) *Synthetic Data Experiment*: We evaluate and quantify the angular resolution limit, the fibre detection success, and the angular errors made during the maxima detection when using the diffusion ODF (dODF) (Eq. 2), our fibre ODF (fODF) (Eq. 6) or the filtered SD (fSD) [13] described in Section III-F1. First, to evaluate angular resolution limits, we generated noise-free synthetic data for two fibres where we varied the crossing angle between fibres to determine the critical

angle at which only a single maximum is detected instead of two. Then, to evaluate fibre detection success, we used noisy synthetic data generated with $\text{SNR} = 35$ and with 1, 2, or 3 fibres chosen randomly with equal volume fractions and random angles between fibres chosen above 45° . We generated 1000 such HARDI profiles separately and counted the number of times we detected the correct ODF maxima. For the simulations, we also varied the estimation order $\ell = 4, 6$ and 8 , used b -values of 1000, 3000 and 5000 s/mm^2 and use sampling densities of $N = 81$ and $N = 321$ on the hemisphere (corresponding to a 3^{rd} and 7^{th} order tessellation of the icosahedron respectively). We also recorded the angular errors made in degrees for each direction. Next, to evaluate the angular error made on the detected maxima, we fixed the fODF and fSD estimation order at $\ell = 6$ and used a simulation with $b = 3000 \text{ s/mm}^2$, $N = 60$ (same gradient directions as our real data acquisition), a separation angle of 60° , a $\text{SNR} = 30$, and a volume fraction $p_1 = p_2 = 0.5$. Finally, we show simulated results that illustrate the effect of varying HARDI signal generation parameters such as b -value, SNR , separation angle and volume fraction. We performed 100 trials of each simulation to assess the effect of noise and we report the mean fibre ODF shape with an opaque surface plus two standard deviations (std) in a transparent surface (also used in [50]). We also show the ground truth fibre directions in blue and the estimated fibre ODF maxima in red colour with slightly longer length in the figures.

3) *Real Data Experiment:* First, we attempt to show the effects of the deconvolution sharpening qualitatively in a region with known fibre crossings between two and three different fibre populations. Then, we compare deterministic tracking methods DT/dODF/fODF/SPLIT-STR and probabilistic dODF/fODF-PROBA on complex fibre bundles. We study the different algorithms to reconstruct several commissural fibre tracts in one subject. Different seed masks were generated on the colour coded FA maps. Fibre tracts and connectivity distributions were generated from every voxel in the mask. For the reconstruction of fibres passing through the anterior commissure (AC), a seed voxel was placed in the mid-sagittal cross-section of the AC and a second tracking was started from two seeds, one on the left and right side of the mid-sagittal cross section. For the commissural fibres connecting the contralateral inferior and middle frontal gyrus a seed voxel was defined in the mid-sagittal section of the rostral body of the CC (Talairach 0, 18, 18). For the tapetum and temporal commissural fibres, we selected four seed voxels between the left lateral ventricle and the optic radiation close to the splenium of the CC (Talairach -22, -42, 24).

4) *Quantifying Lateral Projections of the Corpus Callosum:* As an application of our method, we investigated how the reconstruction of transcallosal fibre connections could be improved with the fODF in the group of eight subjects. We demonstrate in which parts of the CC we can reconstruct fibres connecting the ventral and lateral parts of the cortex. These transcallosal fibres cross the corona radiata and parts of the superior longitudinal fasciculus [56] and cannot be detected well with the simple tensor model or with the dODF. Regions of interest (ROIs) for the white matter tractography in each subject were defined by the sagittal cross section of the CC. For each seed voxel in the ROI, the fODF-PROBA tractography was performed separately. To evaluate the connectivity from the mid-sagittal cross section of the CC to lateral and ventral cortical areas, the percentage of random fibre tracts reaching lateral parts of the brain (Talairach > 30) were quantified. The results were colour coded on the mid-sagittal plane.

IV. RESULTS

A. Deconvolution Sharpening Transformation

[TABLE 1 about here.]

Table I(a) first shows that the angular resolution of QBI is improved with the fibre ODF by approximately 20° over all simulations. The table also shows that fODF has a slightly better angular resolution than fSD [13] (an average of 5° difference in favor of the fODF is observed). The improvement for order $\ell = 8$ is the most apparent with an increase of approximately 25° between fODF and dODF. At order $\ell = 6$, the increase is approximately 15° between fODF and dODF. As expected, the smallest improvement is for lowest order $\ell = 4$, where the ODF is too smooth for the deconvolution sharpening to make an important difference. Moreover, it is expected that the angular resolution will increase considerably for higher b -values. However, note that the difference is very small when comparing the $b = 5000 \text{ s/mm}^2$ and $b = 3000 \text{ s/mm}^2$ columns. Note also that increasing the number of sampling points does not cause any gain in angular resolution in this experiment. There is a difference of only a few degrees when going from sampling $N = 81$ to $N = 321$. This suggests that increasing the number of sampling directions is not important if one uses a low spherical harmonic order estimation. Finally, it is important to point out that when both the dODF and fODF successfully detect the underlying fibre populations, the sharpening does not introduce errors on the detected maxima and actually reduces the systematic error in the dODF, as will be seen in the coming figures.

Table I(b) shows that sharpening increases the success rate of fibre detection in the synthetic data simulation described in Section III-F2. We also see that the fODF and fSD have very similar success rates in this simulation. The fODF has a better success rate than the fSD in some cases because it has a slightly better angular resolution limit. The more important increase in success rate occurs for high estimation order. In particular, for b -value 1000 s/mm^2 , order $\ell = 8$, and sampling $N = 321$, there is an increase of 40% and for $b = 3000 \text{ s/mm}^2$, $\ell = 6$ or 8 , and $N = 81$ there is an increase of more than 30% between fODF and dODF. Note that sharpening the b -value 1000 s/mm^2 data has the effect of improving fibre detection to above the level of b -value 3000 s/mm^2 data without sharpening for most order estimations. This is similarly observed when comparing the dODF column at $b = 5000 \text{ s/mm}^2$ and fODF column at $b = 3000 \text{ s/mm}^2$. Moreover, increasing the spherical sampling density N increases the success rate of fibre detection. This is more apparent at high order $\ell = 8$ and for b -value $> 1000 \text{ s/mm}^2$ for the dODF. Finally, for a given b -value, the fODF column at a low sampling $N = 81$ has a better fibre detection success rate than for the dODF column at high sampling $N = 321$.

[Fig. 2 about here.]

Next, Fig. 2 shows the effect of noise on the angular error of detected maxima from fODF and fSD. We do not plot the curve for the dODF as it coincides with the fODF curve. The fSD and fODF curves have similar profiles but we see a small improvement of approximately 1° to 2° in angular error. Note that the ODF maxima are detected using a fine mesh with 1281 sampling points on the hemisphere, giving roughly 4° between each mesh point. Overall, the mean angular error is thus less than an angular sample.

[Fig. 3 about here.]

[Fig. 4 about here.]

[Fig. 5 about here.]

[Fig. 6 about here.]

Finally, Figs. 3 through 6 qualitatively show the effect of varying the HARDI signal parameters on the dODF, fODF and fSD reconstructions for 100 trials. In these synthetic simulations, the tensor profiles were estimated from our real data. We use simulations with $N = 60$, $b = 3000 \text{ s/mm}^2$, separation angle of 60° , and equal volume fraction $p_1 = p_2 = 0.5$ and then we independently varied the b -value, SNR, separation angle and volume fraction. Note that Figures 3 through 6 confirm

quantitative observations made in Tab. I. The angular resolution gain of the fODF over dODF is striking. Also, the fODF profile is overall sharper than the fSD profile. However, it is possible to see that the fODF peak is not always as well aligned with the true direction as it is for the fSD. In particular, Fig. 3 shows the difference in the reconstruction when changing the estimation order ℓ and the b -value. As expected, the best angular resolution is obtained for high ℓ and b -value. However, for $\ell = 8$, spurious peaks due to noise become more important. We thus choose to fix the order at $\ell = 6$ and $b = 3000 \text{ s/mm}^2$ for the other simulations. Fig. 4 shows that the fODF reconstruction is robust to noise. Even at low SNR, the angular resolution is conserved and the spurious peak effect is not dramatic for $\text{SNR} > 10$. We fixed $\text{SNR} = 30$ for other simulations as in [13]. Fig. 5 qualitatively shows the gain in angular resolution between fSD and fODF. The fODF is able to better discriminate the two fibre compartments at separation angle of 45° and fSD seems limited below a separation angle of 50° . Finally, Fig. 6 shows that the fODF is able to discriminate fibre compartments clearly when the smaller compartment occupies a volume fraction more than 30%. For smaller fractions, only a single compartment is detected. All of these simulations and figures agree with published results in [13], [50], [48].

Therefore, these synthetic simulations indicate that the SDT improves QBI considerably. Our synthetic data simulations show that crossing fibres are more easily detected and that the angular resolution limit is improved with the fODF. The sharpening transformation has the desired effect of enhancing the underlying fibre population, which makes it easier to detect crossing fibre configurations with smaller separation angle. The fODF has a slightly better angular resolution than fSD in some cases because it has a slightly better angular resolution limit.

Fig. 7a qualitatively shows the effect of the deconvolution sharpening transformation on a single voxel of our real dataset. This voxel was selected at the interface between the fibres to the lateral motor stripe and the SLF (Talairach -34 -4 29). We see that the dODF finds only one maximum, but that there seems to be another single fibre compartment with a smaller volume fraction present. The fODF is able to discriminate the second fibre compartment and the recorded separation angle is 62° . As the estimation order increases, the second fibre compartment is more evident, but using such a high order causes the appearance of spurious peaks ($\ell = 8$). We again see that fibre detection and angular resolution are improved when the deconvolution sharpening transformation is used.

[Fig. 7 about here.]

Fig. 7b shows the multidirectional information arising from the diffusion ODF and the fibre ODF in a region of interest in a coronal slice (Talairach -4) of the human brain dataset. In this ROI, the CC forms the roof of the lateral ventricles and fans out in a massive collateral radiation. The corticospinal tract (CST) lies lateral to the ventricle and is directed vertically. The SLF crosses the base of the precentral gyrus in an anterior-posterior direction. The lateral projections of the CC cross the CST and the SLF. Fibres of the SLF partly intersect with the fibres of the CST and the CC. Some voxels of the dODF and fODF in the area (a,a') contain the crossing of these three fibre bundles. It is thus surprising that recent works [3] report no voxels with three crossings. In fact, in the area (a) belonging to this ROI, a large strip of voxels with low FA < 0.15 running at the medial border of the SLF show crossings with three fibre populations as detected in the fODF. Overall, the fODF recovers more voxels with 2-fibre crossings than the dODF. In fact, in a mask of the white-matter, we detect twice as many voxels with two fibre populations with the fODF estimation than with the dODF reconstruction.

B. Tracking

In this section, we compare and study tracking results from the deterministic tracking algorithms, DT-STR, dODF-STR, fODF-STR, and SPLIT-STR from Section III-C, and from the probabilistic tracking algorithms, dODF-PROBA and fODF-PROBA, from Section III-D. The tracking is performed on a synthetic branching data example and on human white matter fibre bundles with known crossings in regions where DT-based algorithms are of limited use. Overall, we observe three results: 1) fODF-PROBA and SPLIT-STR are able to track through fibre crossings and recover crossing, fanning and branching fibre configurations, 2) SPLIT-STR and fODF-PROBA are better than dODF-based and DT-based tracking in regions of fibre crossings, and 3) fODF-PROBA has the classical advantages of probabilistic algorithms over deterministic SPLIT-STR, but is also able to recover many projections from the CC to lateral areas of the cerebral cortex.

1) *Deterministic ODF-based Tracking:* Fig. 8a shows the limitations and differences of DT-STR results compared to fODF-STR and SPLIT-STR results. Tracking was started at the bottom of the branch in all cases. Note that where DTs are prolate with principal directions not agreeing with the true fibre orientations, the ODFs have multiple maxima that match up with the underlying fibre populations. Hence, the path followed by DT-STR is wrong and follows a false direction that takes it

to the middle of the branch. Had there been another structure behind the branching fibres, the tract could have easily leaked into the other structure and diverged. On the other hand, fODF-STR has the advantage of following the right direction. If there are two possible orientations, it goes in direction closest to its incoming direction. In contrast, SPLIT-STR splits and follows both ODF directions when possible which recovers the full branching structure. It is interesting to note the difference between dODF and fODF streamlines in the crossing area. The fODF-STR splitting occurs several voxels lower in the branching where the separation angle between the two fibre compartments is lower than 60° . Finally, we show the tractogram of the fODF-PROBA for three different initialization. The fODF-PROBA is not very sensitive to initialization and is thus able to recover the branching structure starting from voxels at the left, middle, or right of the structure. Note that there is a fanning of tracts from one parallel fibre to the neighbouring fibres within the synthetic bundle. This is expected when using probabilistic tracking and this is why one typically thresholds the tractogram to obtain the most probable tracts.

[Fig. 8 about here.]

Fig. 8b shows a branching fibre configuration in the same ROI as seen in Fig. 7. One set of tracts (red fibres) are started from a voxel in the CC and another set of tracts are started from a voxel in the CST (green/yellow fibres). As expected, SPLIT-STR recovers the branching configuration of both fibre tracts and recovers fibres projecting in motor areas in two gyri. Moreover, fODF-STR is able to step through the crossings that dODF-STR and DT-STR cannot. Both fibres starting from the CST and from the CC take the average direction of the two ODF orientations and project only the medial motor cortex. The angle between fibre compartments is between 60 and 80° in that area and the dODF cannot discriminate clearly the two fibre populations.

2) Probabilistic Tracking:

[Fig. 9 about here.]

Tracking of the anterior commissural (AC) fibres in Fig. 9 shows the advantages of the fODF-PROBA tracking over dODF-PROBA and DT-STR tracking. dODF-PROBA and DT-STR are blocked close to the seed point by low FA areas. Particles of dODF-PROBA cannot propagate to the temporal poles because the paths are diffusive and leak outside the anterior commissural bundle which is only a few voxels wide around the seed point. However, with a multiple seeding approach, DT-STR and dODF-STR are able to recover both paths to the temporal

poles, as published in Catani et al [59]. In contrast, deterministic fODF-STR and SPLIT-STR tracking can reconstruct the fibres connecting the temporal pole via the AC from a single seed point in the mid-sagittal cross section. Probabilistic tractography done with the fODF suggests additional projections to more posterior parts of the temporal lobe and through the anterior subinsular white matter to the inferior occipitofrontal and inferior longitudinal fascicle. Moreover, a second anterior pathway was found on the right hemisphere for this subject (Fig. 9, top row middle and right).

[Fig. 10 about here.]

DT-STR and fODF-STR tracking can only find the commissural fibres connecting the medial parts of the frontal lobe (Fig. 10, second row, left and middle). Fanning of the fibre bundle to the inferior and middle frontal gyrus was found with the SPLIT-STR method on the left hemisphere and to a lesser extent on the right. The tractogram computed with the fODF-PROBA method reveals a strong interhemispheric connection of the lateral parts of the frontal lobe. Additional fibres are found branching to the anterior thalamic radiation (Fig. 10, top left). Fig. 10, top right shows sample fibre tracts included in the probability map (left, middle). We have coloured a selection of the probabilistic fibres in red and blue depending on the end point projections to the lateral and medial areas respectively.

[Fig. 11 about here.]

Fig. 11 shows the fibres in the splenium of the CC which sweep inferior along the lateral margin of the posterior horn of the lateral ventricle that form the tapetum. These fibres are in close contact with the commissural fibres connecting the precuneus of both hemispheres. On the left hemisphere the splitting is close to the four voxel seed region and all methods can bind both parts. Only SPLIT-STR and fODF-PROBA can reconstruct the splitting in both hemispheres to the bundles connecting the temporal lobe and the parietal lobe. The fibres to the temporal lobe split to the transverse temporal (Heschel's) gyrus and to the inferior longitudinal fasciculus. Probabilistic tractography also suggests a close relationship to the posterior thalamic radiation.

C. Quantifying Lateral Projections of the CC

[Fig. 12 about here.]

Fig. 12 shows the colour labelling of the ROI indicating regions with strong lateral connectivity. The colour corresponds to the percentage of fibres which cross a para-sagittal plane (Talairach > 30) as indicated by the lines on the coronal slice. For all subjects, a

maximum number of lateral fibres was found in the genu or the rostral body of the CC connecting the inferior and middle frontal cortex and the premotor cortex. The callosal fibres interdigitate with the fibres of the corona radiata. The tractogram for the voxel with the most lateral connections shows fibres to the left and right middle frontal gyrus and the left inferior frontal gyrus in addition to the connections of the medial frontal cortex. The proportion of lateral fibres in this voxel is $20\% \pm 6\%$ for the eight subjects.

A second peak (see the bright colours) was found in the isthmus or splenium of the CC connecting the temporal areas. The corresponding fibres lie deep to the optic radiation in the tapetum and connect the left and the right temporal lobe and in particular to the left and right auditory cortices. The proportion of temporal fibres in this voxel is $30\% \pm 10\%$ for the eight subjects.

V. DISCUSSION

In this work, we proposed an integral concept for tractography of crossing and splitting fibre bundles based on an estimate of the fibre ODF. We then developed both deterministic and probabilistic tracking methods derived from similar approaches based on DTI. We compared the performances of these algorithms using expert visual validation on complex fibre tracts in a human brain dataset. Moreover, we modelled interhemispheric cortical networks and quantified the projections of the corpus callosum, in particular, to the lateral cortex. In addition, we developed a framework for local modeling linking together the mathematical descriptions of the HARDI signal, the diffusion ODF (dODF) and the fibre ODF (fODF) in a simple and straightforward manner. We demonstrated that the fODF computed by deconvolution of the dODF is very similar to the one obtained by direct spherical deconvolution of the HARDI signals [13]. As a consequence, the angular resolution of QBI can easily be improved by using this simple, linear and analytical sharpening transformation.

The Sharpening Deconvolution Transform and Fibre ODF Reconstruction: The standard Q-ball dODF reconstruction is usually much smoother than one would expect the underlying fibre orientation distribution to be. Even after min-max normalization, the dODF has poor angular resolution, especially at lower b-values. Hence, this is not the best function to work with if one is interested in studying the underlying fibre population. On the other hand, the fODF information is indeed present in the dODF, albeit blurred by the diffusion process. We showed that this blurring can be removed by means of the SDT using a deconvolution kernel representing the dODF of a single fibre. This kernel obviously depends

on the b-value of the HARDI acquisition, whereas the fODF (at least in theory) does not. Hence, as the b-value is increased, the dODF and the deconvolution kernel both become sharper and narrower, rendering dODF and fODF more similar. From this, it is thus clear why the angular resolution of QBI is better for higher b-value acquisitions (provided that the SNR does not change).

The dODF deconvolution kernel is not known exactly, as it depends in a complicated manner on the b-value, the physics of diffusion, the cell membrane permeability, the free diffusion coefficients, the axonal packing, the distribution of axonal diameters, the degree of myelination in the underlying fibre bundles, and other parameters. It has been shown for the classical fSD [13] that potentially incorrect dODF kernels have a moderate effect on the peak amplitudes, without any significant effect on the directions themselves. These results should also apply for our fODF, given the strong parallel between the two methods. In this paper, we used a symmetric dODF kernel estimated directly from real data, which was identical throughout the brain. It is the job of future work to perform the dODF kernel estimation separately at every voxel of the HARDI dataset instead. As our understanding of the relationship between fibre structure and diffusion improves, we will be able to refine the dODF kernel and thus improve the fODF reconstructions.

Currently, there are very few parameters to be chosen in the SDT procedure; the approximation order ℓ of the signal and the regularization parameter [23], [52]. Since the solution only contains linear operations, the fODF estimation is fast and efficient when working with spherical harmonics. The powerful tool we used was the Funk-Hecke theorem, as we used in the derivation of our previous analytical ODF solution [23]. This theorem allows for solving the integral on the sphere between the single fibre dODF kernel and any spherical harmonic.

Note, however, that our fODF estimate is obtained from a concatenation of two operators. First, the HARDI signal is transformed into the dODF, which is then deconvolved in order to obtain the fODF. It is important to point out that in classical HARDI SD [13] and FORECAST [47] algorithms, the fODF or FOD is obtained in a single step by transforming the HARDI signal coefficients directly. Hence, linear SD methods are clearly more direct. The merit of our method lies in the fact that it provides a simple and linear framework for linking the fundamental quantities of the process together, namely MR signal attenuation, diffusion and fibre density, all as a function of direction. It is therefore possible to explicitly study their mutual relationships, particularly between dODF and fODF. The approach provides a new

way to conceptualize spherical deconvolution and may be very appealing to researchers who are only used to thinking in terms of the dODF (e.g. [11], [14], [15], [16], [30], [42], [17]).

In the last year, a number of new SD methods have been developed [47], [46], [48], [49], [50], [22], [4] in order to enhance the robustness and angular resolution of the fODF. However, these methods use non-linear solutions to explicitly deal with spurious peaks and negative diffusion problems and are thus implemented with iterative schemes that are computationally heavy. Only linear methods such as our SDT method, the classical fSD [13] and FORECAST [47] are computationally efficient at the cost of being more vulnerable to negative values on the sphere because they are not explicitly taken into account. In this work, we have compared our new (linear) fODF estimate to the classical fSD [13] and showed that they are in close agreement. The question one might ask is which of these various ways to estimate the fODF yields the best tracking results. Our experience suggests that probabilistic tracking results will ultimately be very similar with each of these different local reconstruction methods, but this remains to be shown in a rigorous way.

Most SD methods suffer from spurious peaks and negative values [4]. There is currently a debate in the literature about whether negative values should be completely removed or not. Some approaches to preventing negative values altogether have been proposed such as the Richardson-Lucy numerical method [48] and a non-negative least squares optimization [4]. Other authors [50] apply a soft constraint to the solution which does allow negative values to occur. Although our approach is not completely immune to negative values appearing on the sphere with the SDT, we have two mechanisms in the fODF estimation that limit these unwanted effects. First, we chose to stick to low order estimations of the ODF, i.e. we use 4th or 6th order spherical harmonics. We observed that the inevitable trade-off between noise in the higher order frequencies and gain in angular resolution is not necessary for our tractography application, especially in the case of probabilistic tracking. In fact, the best results in our real data experiments are obtained for estimation order $\ell = 4$. This also has the advantage of being a very fast fODF estimation (less than 20 seconds on the real dataset) with good compression properties since we only need to store 15 coefficients for every voxel. Note that in [13], [50] the authors mostly consider high estimation orders of $\ell \geq 8$ resulting in the necessity to filter high order frequencies [13] or more recently use a positivity constraint with super-resolution on the spherical deconvolution [50] that also improves their angular resolution. A second

mechanism that limits the effect of spurious peaks in our solution is the Laplace-Beltrami regularization included in the estimation of the spherical harmonic coefficients describing the HARDI signal [23], [52]. This regularization is made in a similar spirit as the gradient constraint regularization recently proposed in [49]. However, note that the former method [49] estimates the optimal regularization parameter at every voxel separately, whereas we have fixed our regularization parameter in order to ensure a fast solution. Our method could be easily adapted to use L-curves as in [52] to estimate the optimal regularization parameter at every voxel which would of course result in a lengthy processing time.

Overall, we have shown that our fODF is robust to spurious peaks and negative values on the sphere by using a low approximation order and a regularization parameter. It is part of our current research to investigate how we can theoretically eliminate negative values and spurious peaks appearing at higher harmonic orders and if it is possible to do so while working directly on the spherical harmonic coefficients without having to project on the sphere and without the need for iterative algorithms such as those used in [50], [48], [4]. A detailed discussion is found in a very recent article about unifying spherical deconvolution methods [4].

Tractography: An important result of the comparison between the different tracking methods is the clear advantage of using the fODF instead of the dODF. We used the fODF and dODF in our extensions of previously DT-based deterministic and probabilistic tracking methods and showed that the fODF clearly outperforms both standard DT-based and dODF-based methods. In the deterministic case, the fODF had a better angular resolution and the maxima of crossing and splitting fibre bundles were detected more easily. We showed that the SPLIT-STR algorithm can follow more multiple maxima and recover most fanning structures in the regions studied. Although sensitive to initialization, SPLIT-STR tracking was able to recover bundles just as well as the fODF-PROBA method in most cases. SPLIT-STR is thus an efficient and easy way to obtain a good idea of fibre tracts starting from only a few seeds. The underlying assumption of SPLIT-STR is that all multiple peaked fODFs represent an underlying branching structure. This makes it reasonable to follow all available maxima at each step. This is the reason for using a curvature threshold of the tracts of 75° instead of 90° . This threshold reduces the chance of following tracts through "pure" crossing configurations where we know that we are then stepping into unwanted fibre bundles. This raises a general question with respect to multidirectional deterministic tractography: Should the tracking algorithm

split so as to recover as much fibre structure as possible before clustering and post-processing the tracts? Alternatively, should the tracking have a built-in scheme to differentiate the different sub-voxel crossing possibilities (e.g. crossing, splitting or kissing) and decide whether or not a tract should be split? Information about the local geometry, curvature and torsion of tracts could help to solve this problem [60] and in [43] promising results are presented taking into account crossing and branching sub-voxel fibre configurations using this local geometry of tracts.

When trying to deal with the uncertainty in the dODF or fODF maxima, the probabilistic approach is more robust. Here, using a fODF instead of a dODF plays a similar role as heuristic tensor sharpening does in probabilistic DTI tracking [27], [34], [44], [45].¹ If one uses the dODF, the tractograms tend to be diffusive and leak into unwanted bundles. However, this leaking effect is not as dominant in probabilistic dODF tracking as it is in probabilistic DTI tracking without sharpening. The min-max normalization of the sampled dODF values to the range between 0 and 1 removes the isotropic part and the shape of the dODF becomes less blurred. However, this technique subtracts a different value in each voxel and hence might introduce artifacts to the tracking result. Moreover, the shape and width of the lobes of the min-max dODF, although sharper than those of the untreated dODF, do not really correspond to the actual fibre distribution in the voxel. On the other hand, the sharper peaks of the fODF, which ideally represents the true fibre directions, improve the spatial localization of the tractograms. The better angular resolution of fODF allows for propagation through crossing, fanning and branching configurations more easily. In our method, we employ an estimate of the fODF that is sampled directly to account for the fact that the fibres in a bundle are not all strictly parallel. Our algorithm follows all possible fibre directions contained in this fODF. It is, however, quite difficult to disentangle the uncertainty and the actual spreading of fibre orientations. We therefore track all directions that are possible given the data and the assumed model assumptions. Other methods use calibration [31], [41], statistical techniques like Markov Chain Monte Carlo [35], [22], and bootstraps [42] to infer a peak uncertainty of the fibre distributions. It remains the purview of future work to compare these different HARDI-based probabilistic tracking methods in a rigorous and systematic way.

Probabilistic tractography yields, in spite of a much

¹Note that this DTI sharpening can also be done with spherical deconvolution applied on the spherical harmonic representation of the diffusion tensor [61].

higher computational load, some major advantages over deterministic approaches. Microscopy of white matter shows that the nerve fibres are not completely parallel even within a bundle. Moreover, bundles might be systematically fanning out. These effects are reflected by a spread around the peaks of the fODF. In contrast to deterministic tractography, which only uses the peaks of the ODF, probabilistic tractography makes use of this spread thereby following more closely the true course of the nerve fibres, which is the case for the fODF, but not for the dODF. The reconstructed fibres spread out to neighbouring voxels within the whole cross section of a fibre bundle, making the algorithm robust to the initialization point. Different starting points within an area entering the same bundle lead to similar tracking results. The spreading of the tractography to the whole bundle enables the segmentation of the selected fibre bundle to its full extent.

Since probabilistic tractography covers all fibres connected to a start voxel, its result, also referred to as a tractogram, represents a connectional fingerprint of a piece of brain tissue contained in a voxel. The information provided by the tractograms can be employed in several ways. By summing the tractograms of several neighbouring seed voxel, one can obtain connectional fingerprints for greater regions (joint tractograms). It is then straightforward to derive quantitative connectivity measures between two different brain regions A and B, e.g. by just integrating the joint tractogram of region A over region B and dividing this by the norm of the entire joint tractogram. Such a measure reflects an estimate of the proportion of the fibres starting in A that reach B (see also [22]). Another use of the tractogram is based on the assumption that the functionality of a neuron or a population of neurons is strongly determined by its pattern of connectivity to the rest of the brain. If seed points are placed in the cortex or at the boundary between the cortex and white matter, the associated tractograms would yield estimates of the global connectivity patterns of the respective pieces of cortex. By using the above hypothesis, one can infer from the connectional similarity between two voxels their functional similarity and thereby parcellate the cortex (or other grey matter structures) into internally homogeneous, but mutually distinct functional-anatomical areas [45]. Finally, tractograms yield a very intuitive representation of the connectivity pattern of the seed point or region when overlaid to anatomical MR slices. Moreover, a 3D rendering of the iso-surface of the probabilistic tractogram gives an overview of the topology and the branching structure of the fibre bundles. On the other hand, it has to be mentioned that probabilistic tractography suffers from connectivity

values that decrease with the distance from the initial seed point due to the fanning of fibre bundles. It is part of our current work to study this problem.

For all these reasons, although slower than SPLIT-STR, we find that fODF-PROBA is more convenient to use for tractography. Overall, the tracking is less sensitive to initialization and the tractogram output more informative than the 3D curves output by SPLIT-STR. fODF-PROBA is thus a very good tool to study specific fibre bundles and compare projections among many subjects. In particular, for fibre tracts that are known to intersect with other bundles like the callosal fibres, DT-based tractography can only reconstruct part of the fibres or might even lead to wrong connections in the intersection position. We were able to show areas of the CC where classical DT-based propagation as well as SPLIT-STR and fODF-STR were limited by their intersection with the corona radiata and the superior longitudinal fasciculus. We showed that we can find fibres from the lateral cortex in a major part of the CC. Current DT-based methods neglect these fibres completely (at least in the frontal lobe), which might lead to wrong interpretations of the white matter architecture of the brain. It is now important to continue this type of experiment and focus on the complex fibre bundles involved in specific functional tasks where DTI tracking is in most cases not very useful.

Acknowledgements: Thanks to Timm Wetzel for providing the diffusion-weighted MR datasets and Enrico Kaden for pre-processing the DWI datasets. Part of this work was supported by PAI Procope. Thanks also to the reviewers who have contributed to improve the quality of the article.

APPENDIX

Let $f(t)$ be continuous on $[-1, 1]$ and Y_ℓ any spherical harmonic of order ℓ in \mathcal{C}^3 , the space of 3D complex functions. Then, given a unit vector \mathbf{u}

$$\int_{|\mathbf{w}|=1} f(\mathbf{u}^T \mathbf{w}) Y_\ell(\mathbf{w}) d\mathbf{w} = \lambda(\ell) Y_\ell(\mathbf{u}), \quad (8)$$

where $\lambda(\ell) = 2\pi \int_{-1}^1 P_\ell(t) f(t) dt$ and P_ℓ the Legendre polynomial of degree ℓ .

Assuming that a Gaussian can describe the diffusion of water molecules for a single fibre, as in DTI, the corresponding diffusion signal that would be measured in direction \mathbf{u} is $S(\mathbf{u}) = e^{-\mathbf{b}\mathbf{u}^T \mathbf{D} \mathbf{u}}$. Without loss of generality, we assume that the fibre is aligned with the z-axis and it has a profile \mathbf{D} with eigenvalues $[e_2, e_2, e_1]$ ($e_1 \gg e_2$). This profile is estimated directly from the real data, taking 300 voxels with highest FA value as we are confident that there is a single fibre population at

those locations. In that case, it is easy to show that the corresponding diffusion ODF, Ψ , is given by

$$\Psi(\mathbf{u}) = \frac{1}{Z} \sqrt{\frac{1}{\mathbf{u}^T \mathbf{D}^{-1} \mathbf{u}}}, \quad (9)$$

where Z is a normalization constant [7], [23]. Now, we have

$$\mathbf{u}^T \mathbf{D}^{-1} \mathbf{u} = \frac{1}{e_2} \sin^2 \theta + \frac{1}{e_1} \cos^2 \theta, \quad (10)$$

where $\mathbf{u} = [x, y, z]^T$ with $x = \cos \phi \sin \theta$, $y = \sin \phi \sin \theta$, $z = \cos \theta$.

$$\begin{aligned} \Psi(\theta) &= \frac{1}{Z} \left(\frac{1}{e_2} \sin^2 \theta + \frac{1}{e_1} \cos^2 \theta \right)^{-\frac{1}{2}} \\ &= \frac{1}{Z} (\cos^2 \theta (e_2 - e_1) + e_1)^{-\frac{1}{2}}. \end{aligned} \quad (11)$$

Letting $t := \cos \theta$ represent the dot product between the direction of the fibre and the point of evaluation, $\Psi(t)$ is defined for $t \in \{-1, 1\}$. This is the domain we need to apply the Funk-Hecke formula to. We thus define the diffusion ODF kernel as

$$R(t) := \Psi(t) = \frac{1}{Z} ((e_2/e_1 - 1)t^2 + 1)^{-\frac{1}{2}} \quad (12)$$

where $Z = \int_{-1}^1 ((e_2/e_1 - 1)t^2 + 1)^{-\frac{1}{2}} dt$. Therefore, the Funk-Hecke integral between diffusion ODF kernel and spherical harmonic of Eqs. 5 and 8 is

$$\lambda(\ell_j) = \frac{2\pi}{Z} \int_{-1}^1 P_{\ell_j}(t) ((e_2/e_1 - 1)t^2 + 1)^{-\frac{1}{2}} dt, \quad (13)$$

which can be solved analytically using MAPLE. Due to the normalization factor Z , the diffusion ODF kernel only depends on the ratio between the eigenvalues, e_2/e_1 . Note that this same Gaussian assumption is used in Anderson [47].

REFERENCES

- [1] S. Mori and P. C. M. van Zijl, "Fiber tracking: principles and strategies - a technical review," *NMR in Biomedicine*, vol. 15, pp. 468–480, 2002.
- [2] P. Basser, J. Mattiello, and D. LeBihan, "Estimation of the effective self-diffusion tensor from the NMR spin echo," *Journal of Magnetic Resonance*, vol. B, no. 103, pp. 247–254, 1994.
- [3] T. E. J. Behrens, H. Johansen-Berg, S. Jbabdi, M. F. S. Rushworth, and M. W. Woolrich, "Probabilistic diffusion tractography with multiple fibre orientations. what can we gain?" *NeuroImage*, vol. 34, no. 1, pp. 144–155, 2007.
- [4] B. Jian and B. C. Vemuri, "A unified computational framework for deconvolution to reconstruct multiple fibers from diffusion weighted mri," *IEEE Transactions on Medical Imaging*, vol. 26, no. 11, pp. 1464–1471, 2007.
- [5] M. Descoteaux, "High angular resolution diffusion mri: from local estimation to segmentation and tractography," Ph.D. dissertation, Université de Nice-Sophia Antipolis, 2008.
- [6] V. Wedeen, T. Reese, D. Tuch, M. Wiesel, J.-G. Dou, R. Weiskoff, and D. Chessler, "Mapping fiber orientation spectra in cerebral white matter with fourier-transform diffusion mri," in *Proceedings of the International Society of Magnetic Resonance in Medicine*. International Society for Magnetic Resonance in Medicine, 2000, p. 82.
- [7] D. Tuch, "Q-ball imaging," *Magnetic Resonance in Medicine*, vol. 52, no. 6, pp. 1358–1372, 2004.
- [8] Y. Assaf and P. Basser, "Composite hindered and restricted model of diffusion (charmed) mr imaging of the human brain," *NeuroImage*, vol. 27, no. 1, pp. 48–58, 2005.
- [9] K. M. Jansons and D. C. Alexander, "Persistent angular structure: new insights from diffusion magnetic resonance imaging data," *Inverse Problems*, vol. 19, pp. 1031–1046, 2003.
- [10] E. Ozarslan, T. Shepherd, B. Vemuri, S. Blackband, and T. Mareci, "Resolution of complex tissue microarchitecture using the diffusion orientation transform (dot)," *NeuroImage*, vol. 31, no. 3, pp. 1086–1103, 2006.
- [11] D. Tuch, "Diffusion mri of complex tissue structure," Ph.D. dissertation, Harvard University and Massachusetts Institute of Technology, 2002.
- [12] C. Liu, R. Bammer, B. Acar, and M. E. Moseley, "Characterizing non-gaussian diffusion by using generalized diffusion tensors," *Magnetic Resonance in Medicine*, vol. 51, pp. 924–937, 2004.
- [13] J.-D. Tournier, F. Calamante, D. Gadian, and A. Connelly, "Direct estimation of the fiber orientation density function from diffusion-weighted mri data using spherical deconvolution," *NeuroImage*, vol. 23, pp. 1176–1185, 2004.
- [14] J. Campbell, K. Siddiqi, V. Rymar, A. Sadikot, and B. Pike, "Flow-based fiber tracking with diffusion tensor q-ball data: Validation and comparison to principal diffusion direction techniques," *NeuroImage*, vol. 27, no. 4, pp. 725–736, Oct. 2005.
- [15] M. Perrin, C. Poupon, Y. Cointepas, B. Rieul, N. Golestani, C. Pallier, D. Riviere, A. Constantinesco, D. L. Bihan, and J.-F. Mangin, "Fiber tracking in q-ball fields using regularized particle trajectories," in *Information Processing in Medical Imaging*, 2005, pp. 52–63.
- [16] J. S. W. Campbell, P. Savadjiev, K. Siddiqi, and G. B. Pike, "Validation and regularization in diffusion mri tractography," in *Third IEEE International Symposium on Biomedical Imaging (ISBI): from Nano to Macro*, Arlington, Virginia, USA, 2006, pp. 351–354.
- [17] V. Wedeen, R. Wang, J. Schmahmann, T. Benner, W. Tseng, G. Dai, D. Pandya, P. Hagmann, H. D'Arceuil, and A. de Crespigny, "Diffusion spectrum magnetic resonance imaging (dsi) tractography of crossing fibers," *NeuroImage*, vol. 41, no. 4, pp. 1267–1277, July 2008.
- [18] G. J. M. Parker and D. C. Alexander, "Probabilistic anatomical connectivity derived from the microscopic persistent angular structure of cerebral tissue," *Philosophical Transactions of the Royal Society, Series B*, vol. 360, pp. 893–902, 2005.
- [19] B. W. Kreher, J. F. Schneider, J. Mader, E. Martin, H. J. and K. Il'yasov, "Multitensor approach for analysis and tracking of complex fiber configurations," *Magnetic Resonance in Medicine*, vol. 54, pp. 1216–1225, 2005.
- [20] W. Guo, Q. Zeng, Y. Chen, and Y. Liu, "Using multiple tensor deflection to reconstruct white matter fiber traces with branching," in *Third IEEE International Symposium on Biomedical Imaging: from Nano to Macro*, Arlington, Virginia, USA, Apr. 2006, pp. 69–72.
- [21] A. Ramirez-Manzanares and M. Rivera, "Basis tensor decomposition for restoring intra-voxel structure and stochastic walks for inferring brain connectivity in dt-mri," *International Journal of Computer Vision*, vol. 69, no. 1, pp. 77 – 92, 2006.
- [22] E. Kaden, T. R. Knosche, and A. Anwander, "Parametric spherical deconvolution: Inferring anatomical connectivity using diffusion mr imaging," *NeuroImage*, vol. 37, pp. 474–488, 2007.
- [23] M. Descoteaux, E. Angelino, S. Fitzgibbons, and R. Deriche, "Regularized, fast, and robust analytical q-ball imaging," *Magnetic Resonance in Medicine*, vol. 58, no. 3, pp. 497–510, 2007.
- [24] S. Mori, B. Crain, V. Chacko, and P. V. Zijl, "Three-dimensional tracking of axonal projections in the brain by Magnetic Resonance Imaging," *Annals of Neurology*, vol. 45, no. 2, pp. 265–269, Feb. 1999.
- [25] T. Conturo, N. Lori, T. Cull, E. Akbudak, A. Snyder, J. Shimony,

- R. McKinsty, H. Burton, and M. Raichle, "Tracking neuronal fiber pathways in the living human brain," *Proceedings of the National Academy of Sciences*, vol. 96, pp. 10 422–10 427, Aug. 1999.
- [26] P. Basser, S. Pajevic, C. Pierpaoli, J. Duda, and A. Aldroubi, "In vivo fiber tractography using DT-MRI data," *Magnetic Resonance in Medicine*, vol. 44, pp. 625–632, 2000.
- [27] M. Lazar, D. Weinstein, J. Tsuruda, K. Hasan, K. Arfanakis, M. Meyerand, B. Badie, H. Rowley, V. Haughton, A. Field, and A. Alexander, "White matter tractography using diffusion tensor deflection," in *Human Brain Mapping*, vol. 18, 2003, pp. 306–321.
- [28] C. Westin, S. Maier, H. Mamata, A. Nabavi, F. Jolesz, and R. Kikinis, "Processing and visualization for diffusion tensor mri," *Medical Image Analysis*, vol. 6, no. 2, pp. 93–108, June 2002.
- [29] Ø. Bergmann, G. Kindlmann, S. Peled, and C.-F. Westin, "Two-tensor fiber tractography," in *4th International Symposium on Biomedical Imaging*, Arlington, Virginia, USA, 2007, pp. 796–799.
- [30] Y.-P. Chao, C.-Y. Yang, K.-H. Cho, C.-H. Yeh, K.-H. Chou, J.-H. Chen, and C.-P. Lin, "Probabilistic anatomical connection derived from qbi with mfact approach," in *International Conference on Functional Biomedical Imaging*, Hangzhou, China, October 2007.
- [31] G. Parker and D. Alexander, "Probabilistic monte carlo based mapping of cerebral connections utilising whole-brain crossing fibre information," in *IPMI*, 2003, pp. 684–695.
- [32] H.-E. Assemlal, D. Tschumperlé, and L. Brun, "Fiber tracking on hardi data using robust odf fields," in *IEEE International Conference on Image Processing*, San Antonio, USA, Sep 2007, pp. 344–351.
- [33] D. K. Jones and C. Pierpaoli, "Confidence mapping in diffusion tensor magnetic resonance imaging tractography using a bootstrap approach," *Magnetic Resonance in Medicine*, vol. 53, pp. 1143–1149, 2005.
- [34] M. Koch, D. Norris, and M. Hund-Georgiadis, "An investigation of functional and anatomical connectivity using magnetic resonance imaging," *NeuroImage*, vol. 16, pp. 241–250, 2002.
- [35] T. E. J. Behrens, M. W. Woolrich, M. Jenkinson, H. Johansen-Berg, R. G. Nunes, S. Clare, P. M. Matthews, J. M. Brady, and S. M. Smith, "Characterization and propagation of uncertainty in diffusion-weighted mr imaging," *Magnetic Resonance in Medicine*, vol. 50, pp. 1077–1088, 2003.
- [36] M. Lazar and A. L. Alexander, "Bootstrap white matter tractography (boot-tract)," *NeuroImage*, vol. 24, pp. 524–532, 2005.
- [37] O. Friman, G. Farneback, and C.-F. Westin, "A bayesian approach for stochastic white matter tractography," *IEEE Transactions in Medical Imaging*, vol. 25, no. 8, 2006.
- [38] C. Lenglet, "Geometric and variational methods for diffusion tensor mri processing," Ph.D. dissertation, Université de Nice-Sophia Antipolis, 2006.
- [39] S. Jbabdi, P. Bellec, R. Toro, J. Daunizeau, M. Pelegrini-Issac, and H. Benali, "Accurate anisotropic fast marching for diffusion-based geodesic tractography," *International Journal of Biomedical Imaging*, vol. 2008, pp. 1–12, 2008.
- [40] S. Jbabdi, M. Woolrich, J. Andersson, and T. Behrens, "A bayesian framework for global tractography," *NeuroImage*, vol. 37, pp. 116–129, 2007.
- [41] K. K. Seunarine, P. A. Cook, M. G. Hall, K. V. Embleton, G. J. M. Parker, and D. C. Alexander, "Exploiting peak anisotropy for tracking through complex structures," in *Mathematical Methods in Biomedical Image Analysis (MMBIA 2007)*, 2007.
- [42] H. A. Haroon and G. J. Parker, "Using the wild bootstrap to quantify uncertainty in fibre orientations from q-ball analysis," in *Proceedings of the International Society of Magnetic Resonance in Medicine*, Berlin, Germany, 19-25th May 2007, p. 903.
- [43] P. Savadjiev, J. S. W. Campbell, M. Descoteaux, R. Deriche, G. B. Pike, and K. Siddiqi, "Labeling of ambiguous sub-voxel fibre bundle configurations in high angular resolution diffusion mri," *NeuroImage*, vol. 41, no. 1, pp. 58–68, 2008.
- [44] J.-D. Tournier, F. Calamante, D. Gadian, and A. Connelly, "Diffusion-weighted magnetic resonance imaging fibre tracking using a front evolution algorithm," *NeuroImage*, vol. 20, pp. 276–288, 2003.
- [45] A. Anwender, M. Tittgemeyer, D. Y. von Cramon, A. D. Friederici, and T. R. Knosche, "Connectivity-based parcellation of broca's area," *Cerebral Cortex*, vol. 17, no. 4, pp. 816–825, 2007.
- [46] D. C. Alexander, "Maximum entropy spherical deconvolution for diffusion mri," in *Image Processing in Medical Imaging*, 2005, pp. 76–87.
- [47] A. Anderson, "Measurements of fiber orientation distributions using high angular resolution diffusion imaging," *Magnetic Resonance in Medicine*, vol. 54, pp. 1194–1206, 2005.
- [48] F. Dell'Acqua, G. Rizzo, P. Scifo, R. Clarke, G. Scotti, and F. Fazio, "A model-based deconvolution approach to solve fiber crossing in diffusion-weighted mr imaging," *IEEE Transactions in Biomedical Engineering*, vol. 54, no. 3, pp. 462–472, 2007.
- [49] K. E. Sakaie and M. J. Lowe, "An objective method for regularization of fiber orientation distributions derived from diffusion-weighted mri," *NeuroImage*, vol. 34, pp. 169–176, 2007.
- [50] J.-D. Tournier, F. Calamante, and A. Connelly, "Robust determination of the fibre orientation distribution in diffusion mri: Non-negativity constrained super-resolved spherical deconvolution," *NeuroImage*, vol. 35, no. 4, pp. 1459–1472, 2007.
- [51] C. Hess, P. Mukherjee, E. Han, D. Xu, and D. Vigneron, "Q-ball reconstruction of multimodal fiber orientations using the spherical harmonic basis," *Magnetic Resonance in Medicine*, vol. 56, pp. 104–117, 2006.
- [52] M. Descoteaux, E. Angelino, S. Fitzgibbons, and R. Deriche, "Apparent diffusion coefficients from high angular resolution diffusion imaging: Estimation and applications," *Magnetic Resonance in Medicine*, vol. 56, pp. 395–410, 2006.
- [53] M. Hlawitschka and G. Scheuermann, "Hot-lines: Tracking lines in higher order tensor fields," in *IEEE Visualization 2005*. Los Alamitos, CA, USA: IEEE Computer Society, Oct. 2005, pp. 27–34.
- [54] D. K. Jones, M. A. Horsfield, and A. Simmons, "Optimal strategies for measuring diffusion in anisotropic systems by magnetic resonance imaging," *Magnetic Resonance in Medicine*, vol. 42, pp. 515–525, 1999.
- [55] D. K. Jones, S. C. R. Williams, D. Gasston, M. A. Horsfield, A. Simmons, and R. Howard, "Isotropic resolution diffusion tensor imaging with whole brain acquisition in a clinically acceptable time," *Human Brain Mapping*, vol. 15, pp. 216–230, 2002.
- [56] J. Talairach and P. Tournoux, *Co-Planar Stereotaxic Atlas of the Human Brain: 3-Dimensional Proportional System : An Approach to Cerebral Imaging*. Thieme Medical Publishers, January 1988.
- [57] M. Jenkinson, P. Bannister, M. Brady, and S. Smith, "Improved optimization for the robust and accurate linear registration and motion correction of brain images," *NeuroImage*, vol. 17, no. 2, pp. 825–841, October 2002.
- [58] FSL, "Fmrib software library," *University of Oxford*, 2006. [Online]. Available: <http://www.fmrib.ox.ac.uk/fsl>
- [59] M. Catani, R. J. Howard, S. Pajevic, and D. K. Jones, "Virtual in vivo interactive dissection of white matter fasciculi in the human brain," *NeuroImage*, vol. 17, pp. 77–94, 2002.
- [60] P. Savadjiev, J. S. W. Campbell, G. B. Pike, and K. Siddiqi, "3d curve inference for diffusion mri regularization and fibre tractography," *Medical Image Analysis*, vol. 10, pp. 799–813, 2006.
- [61] M. Descoteaux, R. Deriche, and C. Lenglet, "Diffusion tensor sharpening improves white matter tractography," in *SPIE Medical Imaging*, San Diego, California, USA, February 2007.

LIST OF TABLES

I	ODF sharpening and spherical deconvolution improve fibre detection and increases angular resolution	
	QBI.	18

TABLE I
ODF SHARPENING AND SPHERICAL DECONVOLUTION IMPROVE FIBRE DETECTION AND INCREASES ANGULAR RESOLUTION QBI.

Angular resolution limitations (a)										
order ℓ	$b = 5000 \text{ s/mm}^2$			$b = 3000 \text{ s/mm}^2$			$b = 1000 \text{ s/mm}^2$			
	fODF	fSD	dODF	fODF	fSD	dODF	fODF	fSD	dODF	
$N = 81$	8	30°	33°	55°	31°	38°	58°	52°	54°	74°
	6	39°	42°	55°	42°	46°	59°	52°	58°	74°
	4	51°	52°	59°	52°	54°	63°	57°	63°	75°
$N = 321$	8	29°	32°	44°	30°	36°	50°	45°	50°	69°
	6	37°	40°	47°	38°	43°	52°	45°	55°	69°
	4	50°	50°	56°	52°	55°	60°	56°	62°	72°
Fibre detection success (b)										
order ℓ	$b = 5000 \text{ s/mm}^2$			$b = 3000 \text{ s/mm}^2$			$b = 1000 \text{ s/mm}^2$			
	fODF	fSD	dODF	fODF	fSD	dODF	fODF	fSD	dODF	
$N = 81$	8	100%	100%	78%	94%	94%	61%	86%	85%	56%
	6	99%	99%	76%	91%	90%	60%	69%	67%	54%
	4	70%	70%	62%	63%	63%	55%	62%	60%	52%
$N = 321$	8	100%	100%	96%	100%	100%	87%	95%	95%	55%
	6	100%	100%	88%	100%	100%	84%	66%	70%	53%
	4	83%	83%	62%	78%	76%	62%	58%	56%	52%

LIST OF FIGURES

1	Sketch of the convolution/deconvolution process. In (a), the convolution between the diffusion ODF kernel R and the fibre orientation function (FOD) produces a smooth diffusion ODF Ψ . In (b), we show a sketch of the deconvolution sharpening. The Funk-Radon Transform of the simulated HARDI signal on the sphere S produces a smooth diffusion ODF Ψ . This diffusion ODF is transformed into a sharper fibre ODF Ψ_{sharp} by deconvolution with the diffusion ODF kernel R of (a).	21
2	Effect of varying SNR on the detected maximum of the fibre ODF (fODF) and filtered spherical deconvolution (fSD) [13]. We plot the mean and standard deviation of the estimated angle error for the fibre simulation with separation angle of 60° , $b = 3000$ s/mm ² and $N = 81$	22
3	Effect of varying estimation order ℓ and b -value on the diffusion ODF (dODF), fibre ODF (fODF) and filtered spherical deconvolution (fSD) [13]. The opaque surface corresponds to the mean FOD over 100 noise trials, whereas the transparent surface corresponds to the mean plus two standard deviations. Blue and red lines correspond to ground truth fibre directions and detected maxima respectively. . .	23
4	Effect of varying SNR on the diffusion ODF (dODF), fibre ODF (fODF) and filtered spherical deconvolution (fSD) [13]. The opaque surface corresponds to the mean FOD over 100 trials that include random noise, whereas the transparent surface corresponds to the mean plus two standard deviations. Blue and red lines correspond to ground truth fibre directions and detected maxima, respectively. . .	24
5	Effect of varying separation angle on the diffusion ODF (dODF), fibre ODF (fODF) and filtered spherical deconvolution (fSD) [13]. The opaque surface corresponds to the mean FOD over 100 trials with random noise, whereas the transparent surface corresponds to the mean plus two standard deviations. Blue and red lines correspond to ground truth fibre directions and detected maxima respectively.	25
6	Effect of varying volume fraction on the diffusion ODF (dODF), fibre ODF (fODF) and filtered spherical deconvolution (fSD) [13]. The opaque surface corresponds to the mean FOD over 100 trials with random noise, whereas the transparent surface corresponds to the mean plus two standard deviations. Blue and red lines correspond to ground truth fibre directions and detected maxima respectively.	26
7	Deconvolution sharpening on real data improves fibre detection of QBI by increasing angular resolution. In the (1), the second maximum is missed in the diffusion ODF (dODF) and min-max normalized dODF. With sharpening, the second fibre direction is identified even at the low orders of $\ell = 4$ and $\ell = 6$. The real data voxel in (a) was manually selected by an expert at the interface between motor stripe and superior longitudinal fasciculus. In (b), there are more crossings detected using the fibre ODF (a,b) than dODF (a',b'). The ROI shows crossings between the cortical spinal tract/corona radiata (cst/cr) (going up in the plane), superior longitudinal fibres (slf) (coming out of the plane) and the lateral projections of the corpus callosum (cc) (in the plane). (a,a') are tilted so that the fibre directions can be more clearly seen.	27
8	SPLIT-STR is able to recover the known fibre fanning configurations. In (a), deterministic tracking was started at the bottom of the branch in all cases. HARDI data was generated with b -value of 3000 s/mm ² , $N = 81$ and SNR = 35. fODF-PROBA was also performed with 3 different initializations overlaid on the DT principal eigenvector. fODF-PROBA is not particularly sensitive to initialization. In (b), SPLIT-STR recovers known branching configurations to the two motor gyri from both seed points. We have coloured fibres starting from the CC in red and fibres starting from the CST in green/yellow.	28
9	Tracking of the anterior commissure fibres (ac). Probabilistic tracking is shown on coronal and axial slices through the ac. We also show a 3D rendering of the tractogram iso-surface. fODF-Proba reaches the temporal pole close to the uncinate fasciculus (unc) whereas dODF-Proba can only reconstruct a small part. Deterministic tractography needs multiple seeding initialization in the DT and dODF cases due to the small diameter of the ac on this subject.	29

10	Tracking of the projections of the corpus callosum to Broca's area. The probabilistic tractogram is shown on a coronal and sagittal slice and as 3D rendering. The tractogram shows asymmetry with stronger connections to the left inferior and middle frontal gyrus than to the homologue area. We also show a selection of the probabilistic fibres (fODF-PROBA) coloured differently depending on their end point projections to the lateral (red) or medial areas (blue). From the deterministic methods, only SPLIT-STR can reconstruct this complex structure.	30
11	Probabilistic tractogram of a single seed point in the tapetum (tap) reconstructs the fibres crossing the cc and connecting both temporal lobes. Deterministic tracking was initialized from 4 seed points in the tapetum. SPLIT-STR reconstructed this complex structure.	31
12	Quantification of the ratio of lateral fibres (Talairach > 30) in the different parts of the corpus callosum (cc) typically completely missed in DT tractography. All 8 subjects show strong lateral connectivity in the genu or the rostral body of the cc and a second peak in the splenium. fODF-PROBA finds more than 10% of lateral fibres in large parts of the cc.	32

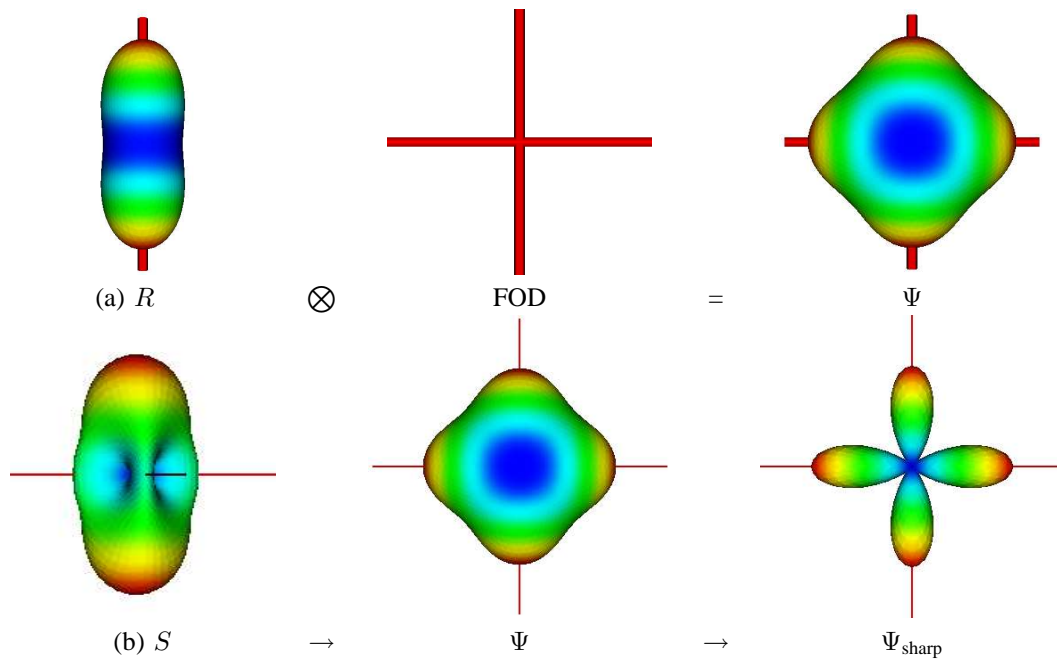


Fig. 1. Sketch of the convolution/deconvolution process. In (a), the convolution between the diffusion ODF kernel R and the fibre orientation function (FOD) produces a smooth diffusion ODF Ψ . In (b), we show a sketch of the deconvolution sharpening. The Funk-Radon Transform of the simulated HARDI signal on the sphere S produces a smooth diffusion ODF Ψ . This diffusion ODF is transformed into a sharper fibre ODF Ψ_{sharp} by deconvolution with the diffusion ODF kernel R of (a).

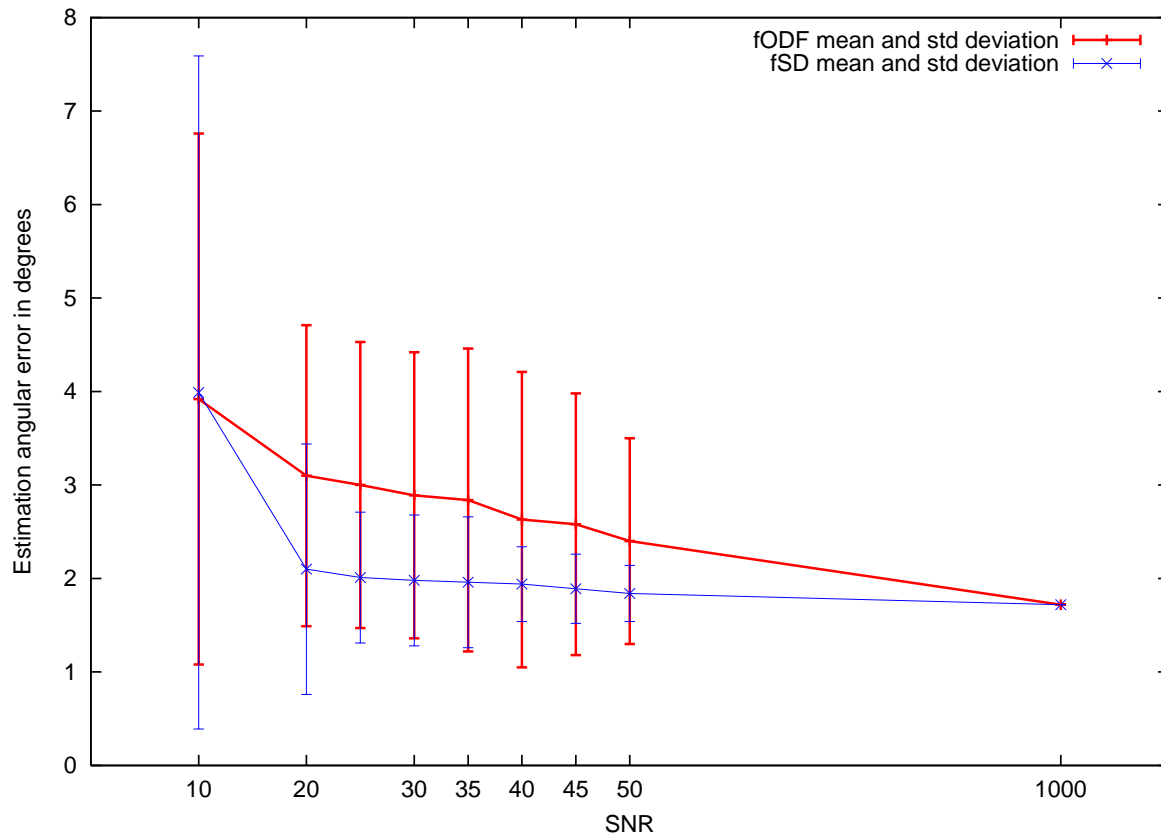


Fig. 2. Effect of varying SNR on the detected maximum of the fibre ODF (fODF) and filtered spherical deconvolution (fSD) [13]. We plot the mean and standard deviation of the estimated angle error for the fibre simulation with separation angle of 60° , $b = 3000 \text{ s/mm}^2$ and $N = 81$.

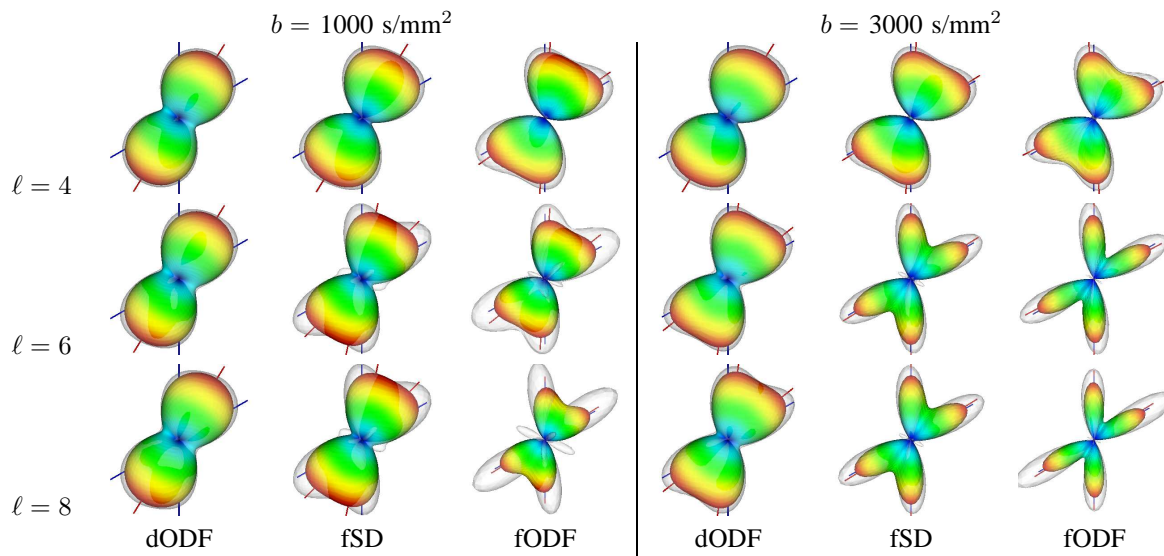


Fig. 3. Effect of varying estimation order ℓ and b -value on the diffusion ODF (dODF), fibre ODF (fODF) and filtered spherical deconvolution (fSD) [13]. The opaque surface corresponds to the mean FOD over 100 noise trials, whereas the transparent surface corresponds to the mean plus two standard deviations. Blue and red lines correspond to ground truth fibre directions and detected maxima respectively.

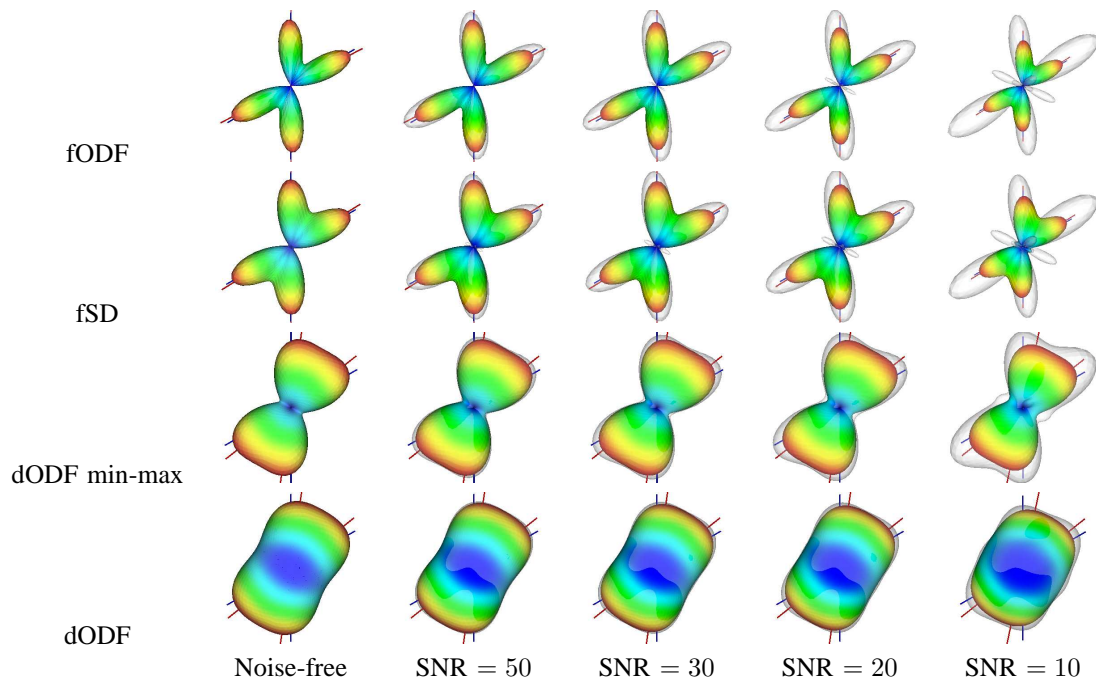


Fig. 4. Effect of varying SNR on the diffusion ODF (dODF), fibre ODF (fODF) and filtered spherical deconvolution (fSD) [13]. The opaque surface corresponds to the mean FOD over 100 trials that include random noise, whereas the transparent surface corresponds to the mean plus two standard deviations. Blue and red lines correspond to ground truth fibre directions and detected maxima, respectively.

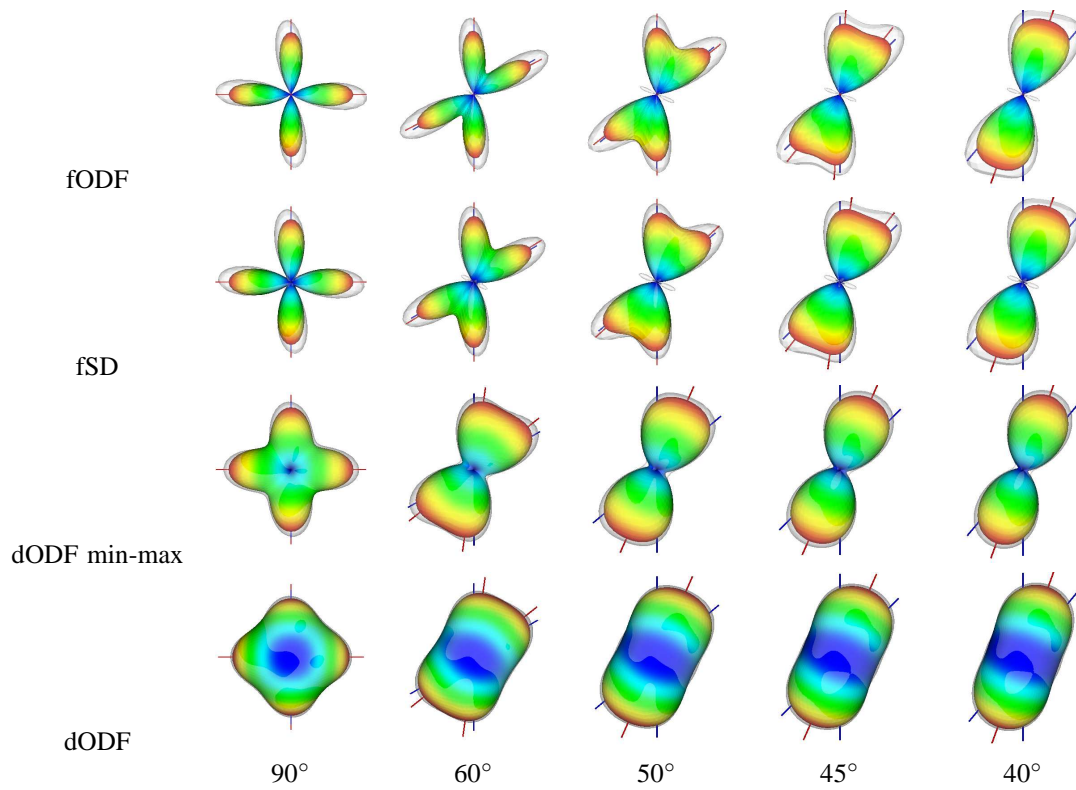


Fig. 5. Effect of varying separation angle on the diffusion ODF (dODF), fibre ODF (fODF) and filtered spherical deconvolution (fSD) [13]. The opaque surface corresponds to the mean FOD over 100 trials with random noise, whereas the transparent surface corresponds to the mean plus two standard deviations. Blue and red lines correspond to ground truth fibre directions and detected maxima respectively.

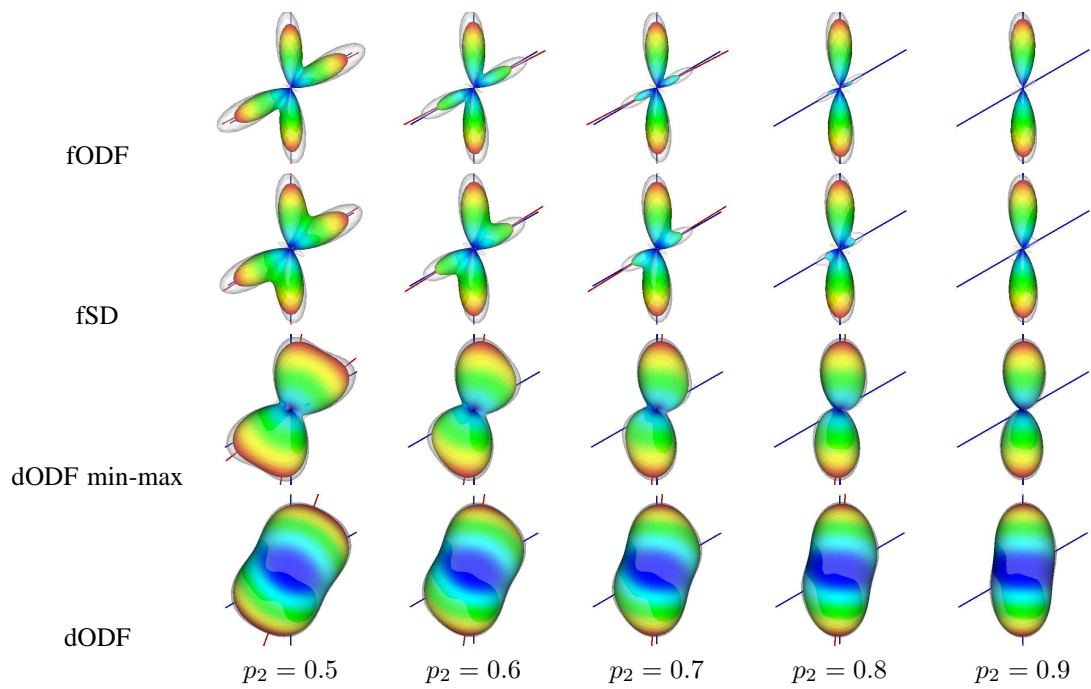


Fig. 6. Effect of varying volume fraction on the diffusion ODF (dODF), fibre ODF (fODF) and filtered spherical deconvolution (fSD) [13]. The opaque surface corresponds to the mean FOD over 100 trials with random noise, whereas the transparent surface corresponds to the mean plus two standard deviations. Blue and red lines correspond to ground truth fibre directions and detected maxima respectively.

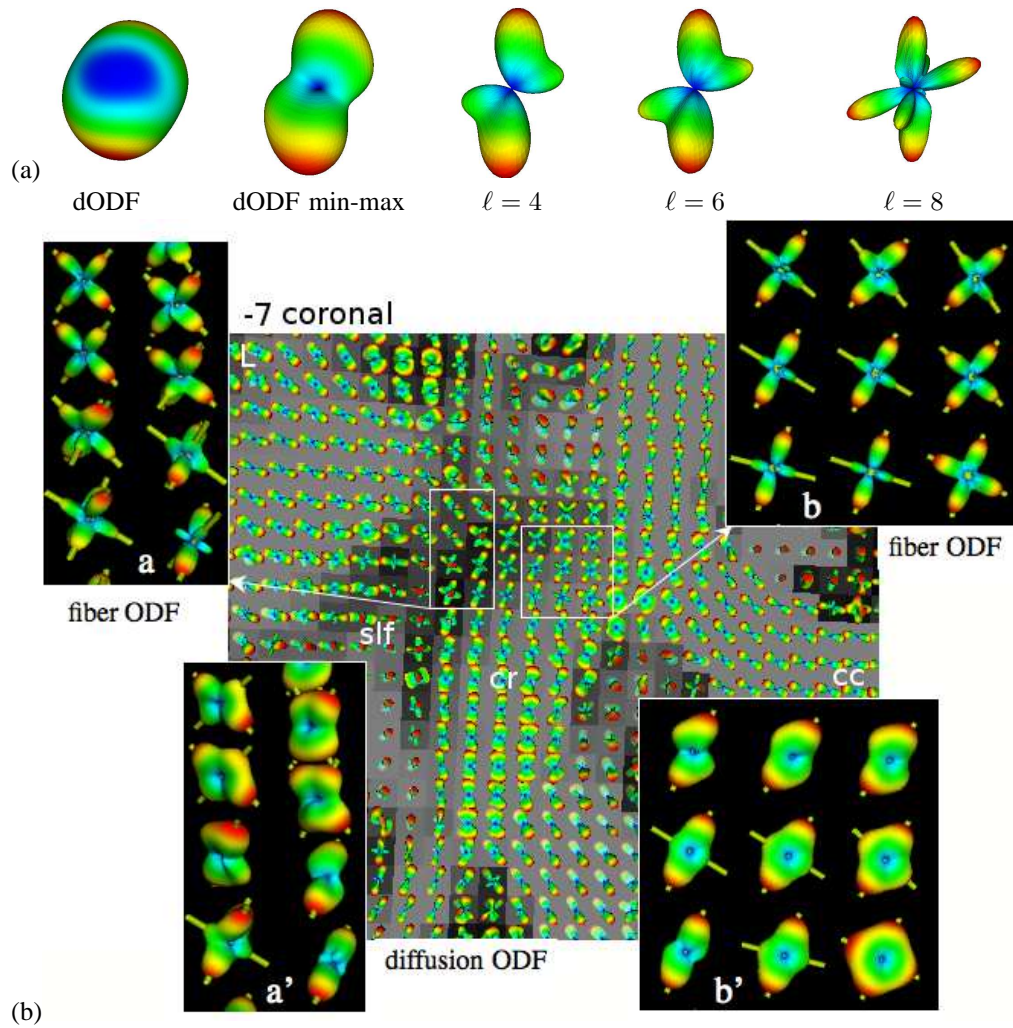


Fig. 7. Deconvolution sharpening on real data improves fibre detection of QBI by increasing angular resolution. In the (1), the second maximum is missed in the diffusion ODF (dODF) and min-max normalized dODF. With sharpening, the second fibre direction is identified even at the low orders of $\ell = 4$ and $\ell = 6$. The real data voxel in (a) was manually selected by an expert at the interface between motor stripe and superior longitudinal fasciculus. In (b), there are more crossings detected using the fibre ODF (a,b) than dODF (a',b'). The ROI shows crossings between the cortical spinal tract/corona radiata (cst/cr) (going up in the plane), superior longitudinal fibres (slf) (coming out of the plane) and the lateral projections of the corpus callosum (cc) (in the plane). (a,a') are tilted so that the fibre directions can be more clearly seen.

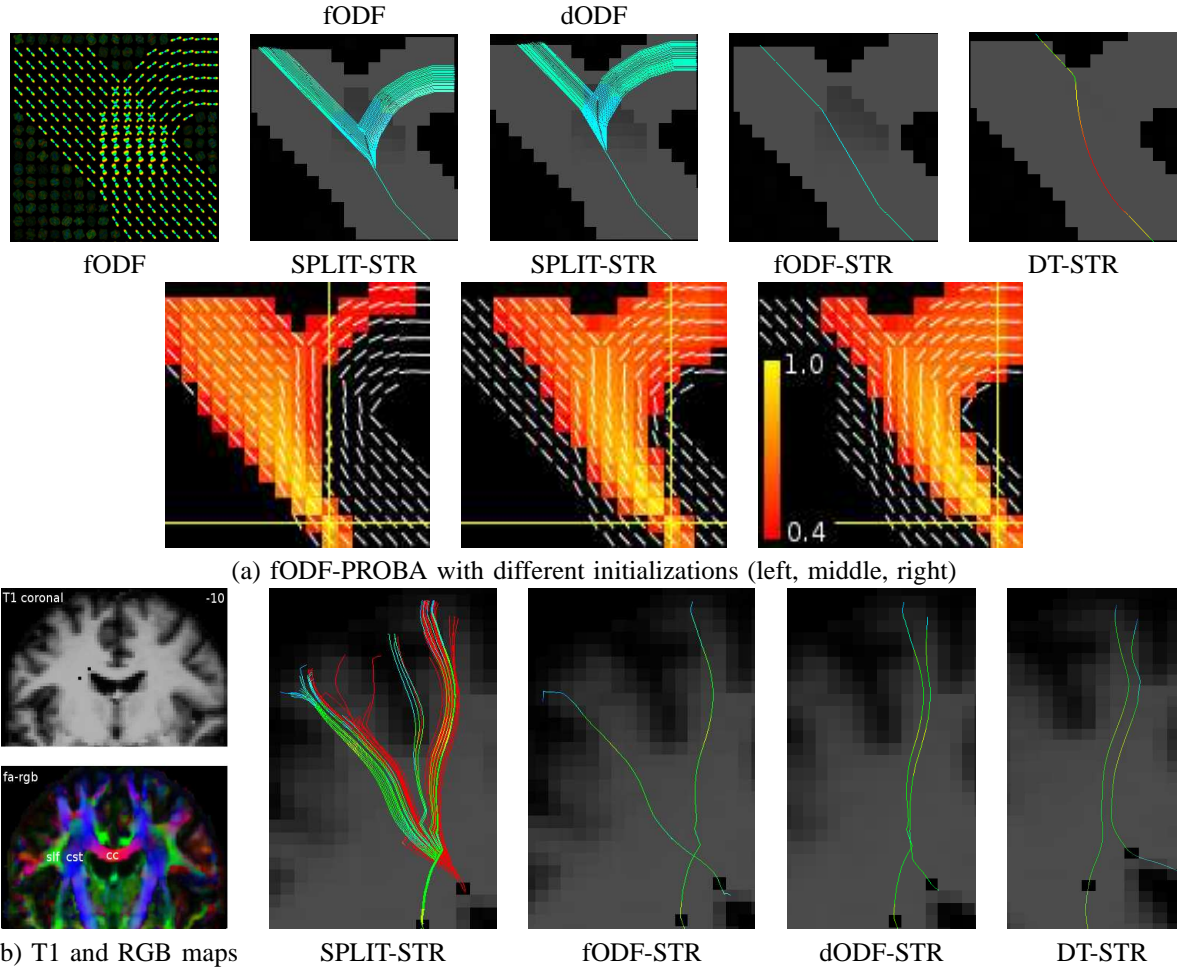


Fig. 8. SPLIT-STR is able to recover the known fibre fanning configurations. In (a), deterministic tracking was started at the bottom of the branch in all cases. HARDI data was generated with b -value of 3000 s/mm^2 , $N = 81$ and $\text{SNR} = 35$. fODF-PROBA was also performed with 3 different initializations overlaid on the DT principal eigenvector. fODF-PROBA is not particularly sensitive to initialization. In (b), SPLIT-STR recovers known branching configurations to the two motor gyri from both seed points. We have coloured fibres starting from the CC in red and fibres starting from the CST in green/yellow.

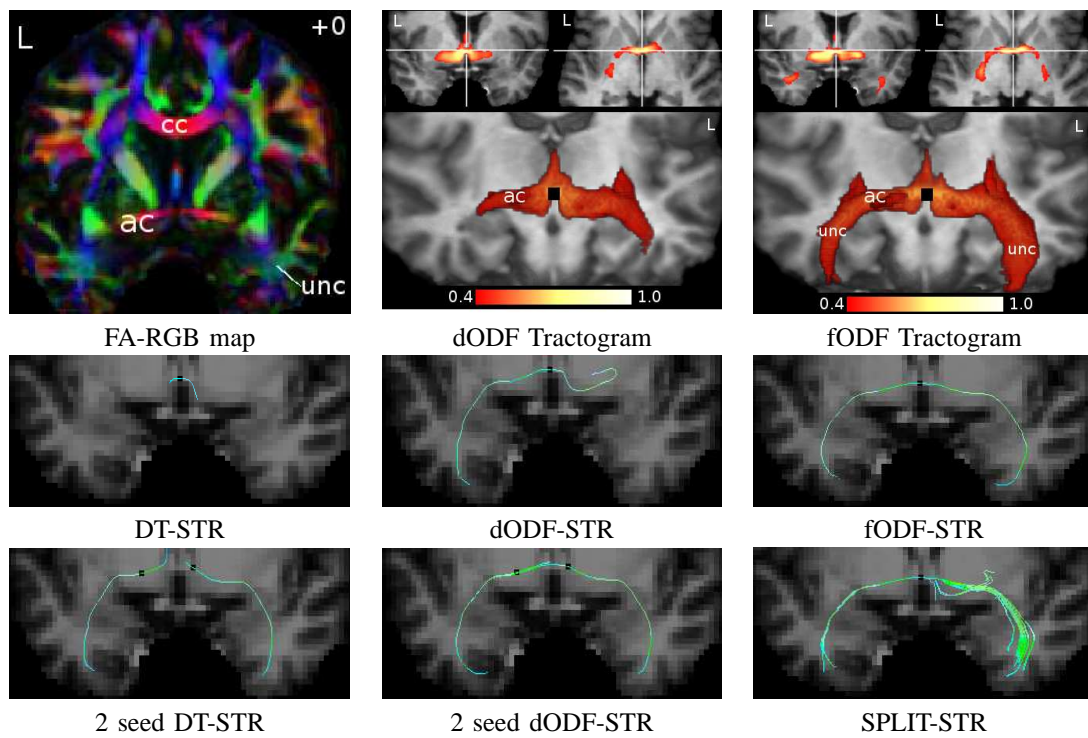


Fig. 9. Tracking of the anterior commissure fibres (ac). Probabilistic tracking is shown on coronal and axial slices through the ac. We also show a 3D rendering of the tractogram iso-surface. fODF-Proba reaches the temporal pole close to the uncinate fasciculus (unc) whereas dODF-Proba can only reconstruct a small part. Deterministic tractography needs multiple seeding initialization in the DT and dODF cases due to the small diameter of the ac on this subject.

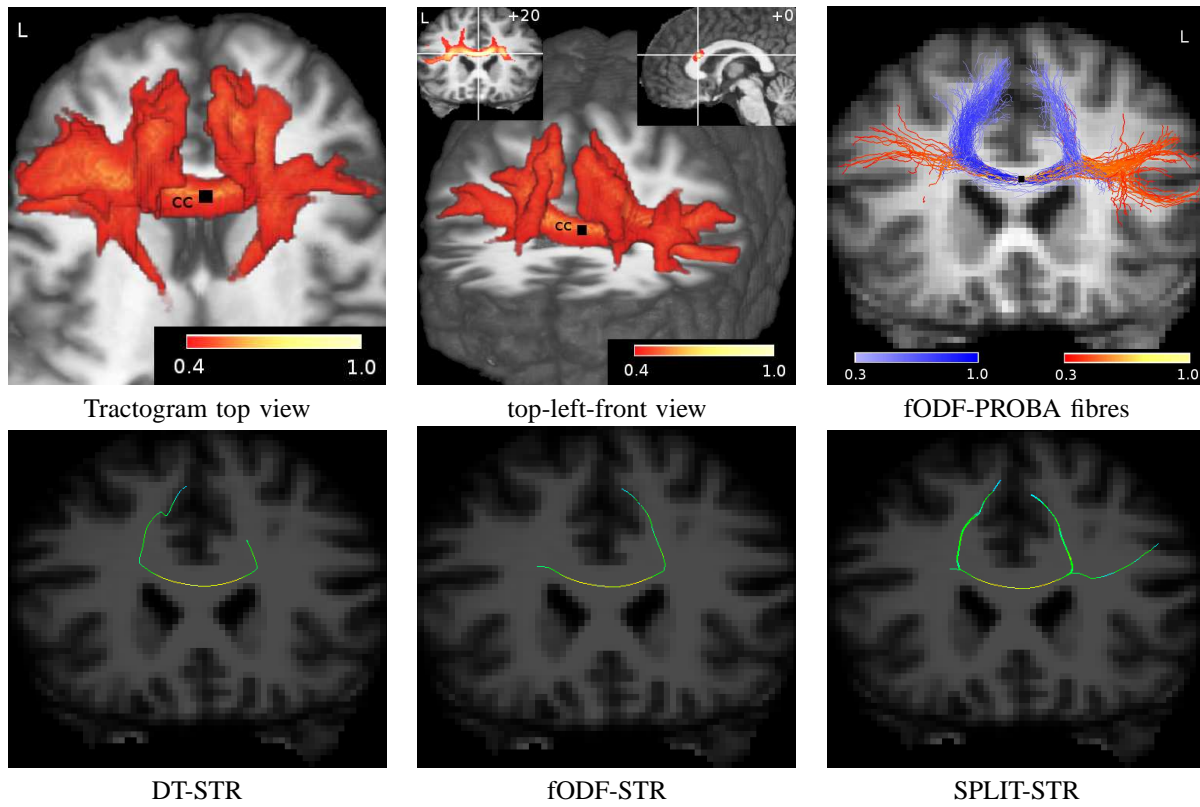


Fig. 10. Tracking of the projections of the corpus callosum to Broca's area. The probabilistic tractogram is shown on a coronal and sagittal slice and as 3D rendering. The tractogram shows asymmetry with stronger connections to the left inferior and middle frontal gyrus than to the homologue area. We also show a selection of the probabilistic fibres (fODF-PROBA) coloured differently depending on their end point projections to the lateral (red) or medial areas (blue). From the deterministic methods, only SPLIT-STR can reconstruct this complex structure.

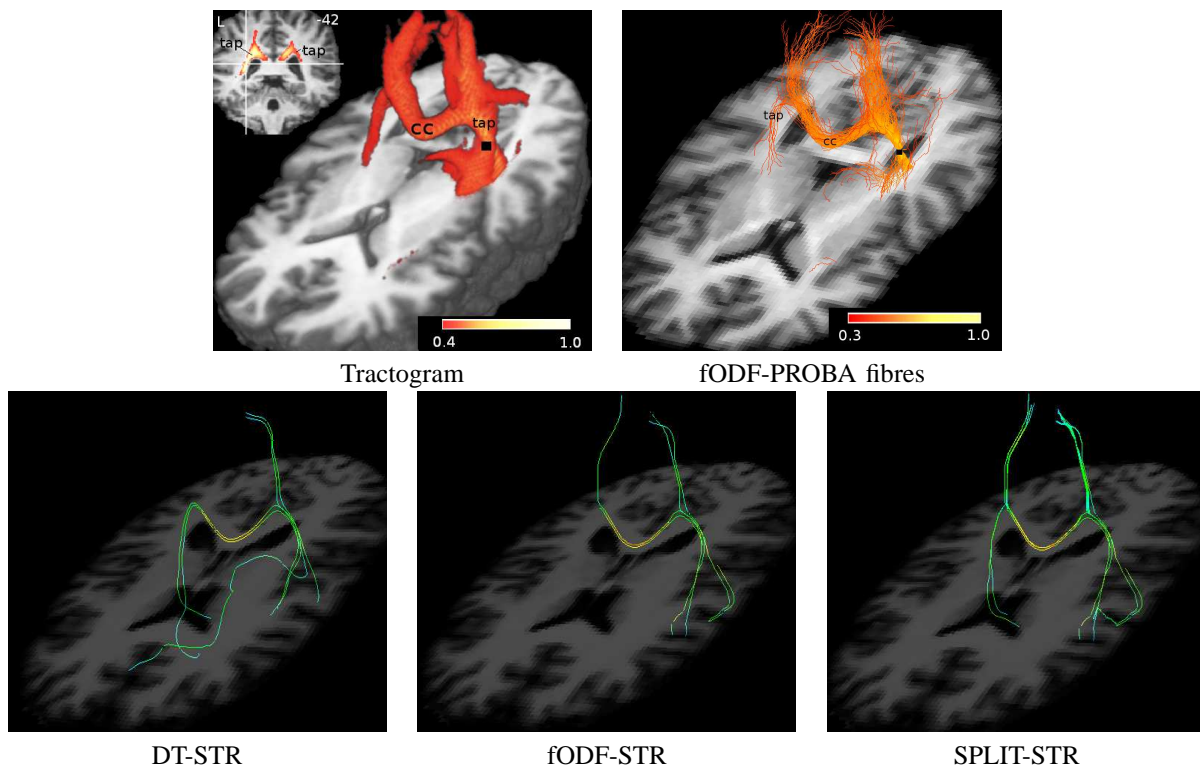


Fig. 11. Probabilistic tractogram of a single seed point in the tapetum (tap) reconstructs the fibres crossing the cc and connecting both temporal lobes. Deterministic tracking was initialized from 4 seed points in the tapetum. SPLIT-STR reconstructed this complex structure.

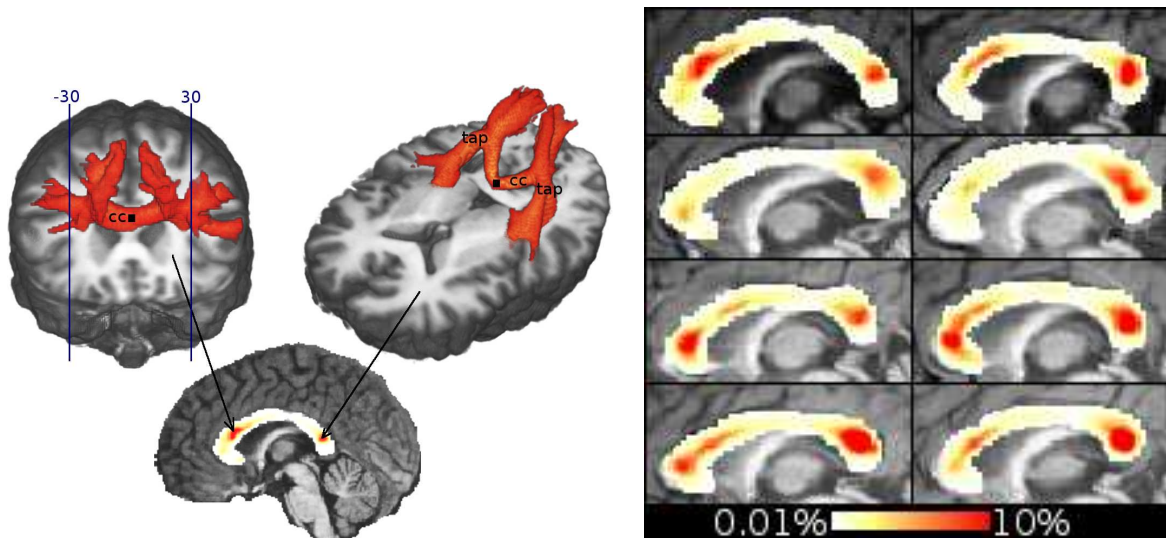


Fig. 12. Quantification of the ratio of lateral fibres (Talairach > 30) in the different parts of the corpus callosum (cc) typically completely missed in DT tractography. All 8 subjects show strong lateral connectivity in the genu or the rostral body of the cc and a second peak in the splenium. fODF-PROBA finds more than 10% of lateral fibres in large parts of the cc.